REPORT DOCUMENTATION PAGE

Form Approved OMB NO. 0704-0188

1. REPORT DATE (DD-MM-YYYY)	2. REPORT TYPE	3. DATES COVERED (From - To)
	New Reprint	-

4. TITLE AND SUBTITLE	5a. CONTRACT NUMBER
Blind experimental data collected in the field and an approximately globally convergent inverse algorithm	W911NF-11-1-0399
	5b. GRANT NUMBER
	5c. PROGRAM ELEMENT NUMBER
	611102

6. AUTHORS	5d. PROJECT NUMBER
Andrey V. Kuzhuget, Larisa Beilina, Michael V. Klibanov, Anders Sullivan, Lam Nguyen	
	5e. TASK NUMBER
	5f. WORK UNIT NUMBER

7. PERFORMING ORGANIZATION NAMES AND ADDRESSES	8. PERFORMING ORGANIZATION REPORT NUMBER
University of North Carolina - Charlotte Office of Sponsored Programs 9201 University City Blvd. Charlotte, NC 28223 -0001	

9. SPONSORING/MONITORING AGENCY NAME(S) AND ADDRESS(ES)	10. SPONSOR/MONITOR'S ACRONYM(S)
U.S. Army Research Office P.O. Box 12211 Research Triangle Park, NC 27709-2211	ARO
	11. SPONSOR/MONITOR'S REPORT NUMBER(S)
	60035-MA.4

12. DISTRIBUTION AVAILIBILITY STATEMENT

Approved for public release; distribution is unlimited.

13. SUPPLEMENTARY NOTES

The views, opinions and/or findings contained in this report are those of the author(s) and should not contrued as an official Department of the Army position, policy or decision, unless so designated by other documentation.

14. ABSTRACT

An approximately globally convergent numerical method for a 1-D Coefficient Inverse Problem for a hyperbolic PDE is applied to image dielectric constants of targets from blind experimental data. The data were collected in the field by the Forward Looking Radar of the US Army Research Laboratory. A posteriori analysis has revealed that computed and tabulated values of dielectric constants are in a good agreement. Convergence analysis is presented.

15. SUBJECT TERMS

globally convergent inverse algorihm, blind experimental data, convergence analysis, accurate imaging of dielectric constants of five our of five targets, joint publication with ARL engineers (A. Sullivan and L. Ngueyn)

16. SECURITY CLASSIFICATION OF:			17. LIMITATION OF ABSTRACT	15. NUMBER OF PAGES	19a. NAME OF RESPONSIBLE PERSON
a. REPORT	b. ABSTRACT	c. THIS PAGE			Michael Klibanov
UU	UU	UU	UU		19b. TELEPHONE NUMBER
					704-687-2645

Report Title

Blind experimental data collected in the field and an approximately globally convergent inverse algorithm

ABSTRACT

An approximately globally convergent numerical method for a 1-D Coefficient Inverse Problem for a hyperbolic PDE is applied to image dielectric constants of targets from blind experimental data. The data were collected in the field by the Forward Looking Radar of the US Army Research Laboratory. A posteriori analysis has revealed that computed and tabulated values of dielectric constants are in a good agreement. Convergence analysis is presented.

REPORT DOCUMENTATION PAGE (SF298)
(Continuation Sheet)

Continuation for Block 13

ARO Report Number   60035.4-MA
Blind experimental data collected in the field and   ...

Block 13: Supplementary Note

Blind backscattering experimental data collected in the field and an approximately globally convergent inverse algorithm

Andrey V Kuzhuget (UNCC/ChalmersGU team)[1,6],
Larisa Beilina (UNCC/ChalmersGU team)[2],
Michael V Klibanov (UNCC/ChalmersGU team)[3,7],
Anders Sullivan (ARL Team)[4]**, Lam Nguyen (ARL Team)**[4]
and Michael A Fiddy (UNCC/ChalmersGU team)[5]

[1] Morgan Stanley & Co. Incorporated, 1585 Broadway, New York, NY 10036, USA
[2] Department of Mathematical Sciences, Chalmers University of Technology and Gothenburg University, SE-42196 Gothenburg, Sweden
[3] Department of Mathematics and Statistics, University of North Carolina at Charlotte, Charlotte, NC 28223, USA
[4] US Army Research Laboratory, 2800 Powder Mill Road Adelphy, MD 20783-1197, USA
[5] Optoelectronics Center, University of North Carolina at Charlotte, Charlotte, NC 28223, USA

E-mail: larisa@chalmers.se, mklibanv@uncc.edu, anders.j.sullivan.civ@mail.mil, lam.h.nguyen2.civ@mail.mil and mafiddy@uncc.edu

Abstract

An approximately globally convergent numerical method for a 1D coefficient inverse problem for a hyperbolic PDE is applied to image dielectric constants of targets from blind experimental data. The data were collected in the field by the Forward Looking Radar of the US Army Research Laboratory. *A posteriori* analysis has revealed that computed and tabulated values of dielectric constants are in good agreement. Convergence analysis is presented.

(Some figures may appear in colour only in the online journal)

1. Introduction

In this paper, we test the 1D version [30] of the numerical method of recent publications [5–12, 26, 27, 31, 47] for the case when the time-resolved backscattering electric signal is measured experimentally in the field. Measurements were performed by the Forward Looking Radar built in the US Army Research Laboratory (ARL). All kinds of clutters were present at

---

[6] Formerly with University of North Carolina, Charlotte, NC, USA.
[7] Author to whom any correspondence should be addressed.

the site of data collection. The data are severely limited. The goal of this radar is to detect and possibly identify shallow explosive-like targets. Prior to this effort, the focus of the ARL team was on the image processing rather than on the target detection and identification [36]. The current data processing procedure of ARL delivers only the energy information. The algorithm of this paper computes values of dielectric constants of targets using those data. These values represent a new, surprising and quite useful dimension of information for the ARL team. A hope is that these values might be helpful in the target detection and identification process.

The UNCC/ChalmersGU team has worked only with the most challenging case of *blind* experimental data. 'Blind' means that first computations were made by the UNCC/ChalmersGU team without any knowledge of correct answers. Next, computational results were sent to the ARL team. The ARL team has compared *a posteriori* those results with the reality and then revealed correct answers to the UNCC/ChalmersGU team.

In the above cited works, a new numerical method was developed for some multidimensional coefficient inverse problems (MCIPs) for a hyperbolic PDE with single measurement data. 'Single measurement' means that either only a single position of the point source or only a single direction of the incident plane wave is considered. Because of many dangers on the battlefield, the single measurement arrangement is the most suitable one for military applications. There were two goals of those publications.

Goal 1. To develop such a numerical method, which would have a rigorous guarantee obtaining a good approximation for the exact solution of a coefficient inverse problem (CIP) without using advanced knowledge of either a small neighborhood of that solution or of the background medium in the domain of interest.

Goal 2. This method should demonstrate a good performance on both computationally simulated and experimental data.

It is well known that it is *enormously challenging* to achieve both goals 1 and 2 simultaneously. Three substantial obstacles are combined here: the minimal information content due to the single source only, nonlinearity and ill-posedness. Therefore, it was inevitable in the above-cited publications to introduce some natural approximations. Although those approximations cannot be rigorously justified sometimes, still they have resulted in the simultaneous achievement of both goals; see more details in sections 4 and 6. The numerical methods of [5–12, 26, 27, 30, 31, 47] use the structure of the underlying PDE operator rather than a least-squares functional. The above thoughts are reflected in the following statement of the review paper [12] 'The key philosophical focus of our review is the above point about natural assumptions/approximations which make the technique numerically efficient.'

Because of the measurement scheme of the Forward Looking Radar, the UNCC/ChalmersGU team had only one time-resolved curve for each target. This curve was the voltage averaged over some readings (section 7). Only one component of the electric field was generated and measured in the backscattering regime. The reality is 3D, and the electric field propagation is governed by the full Maxwell system. However, the above data structure has left us with no choice but to model the process by a 1D CIP using only one hyperbolic PDE.

The main challenge of working with these data was a *huge misfit* between them and computationally simulated data, e.g. compare figure 3(b) with figures 4(b), (d) and (f). Namely, the experimentally measured curves are highly oscillatory, unlike the computed ones. Therefore, to make the experimental data suitable for the inversion, we apply a new data pre-processing procedure, which is a crucial step. This procedure was unbiased, since we have worked with the blind data only. See [10, 26] and chapter 5 of [6] for a similar data pre-processing procedure for the case of transmitted experimental data. Both these procedures

are based on the intuition only. The only justification for both is the accuracy of obtained results; see also comments in section 9 below.

There are some classical numerical methods of solving 1D CIPs for hyperbolic equations; see, e.g. [19, 25, 35] and references therein. However, because of many uncertainties in our experimental data, including the above misfit and the 3D reality versus the 1D mathematical model (also, see subsection 7.2), it is yet unclear how those methods would perform for our data. This question deserves a separate research effort.

There are also MCIPs with multiple measurement data. 'Multiple measurements' means that the data are generated either by the point source running along a manifold, or by the incident plane wave, whose direction varies within a certain cone. These MCIPs have applications in medical imaging. We refer to [1, 13, 16, 17, 21, 24, 37–40] for some non-local reconstruction techniques for these MCIPs. An analogue of the technique of [5] for the case of a 2D CIP for an elliptic PDE with the source running along a straight line was developed [28, 41, 42]. Validation of the latter for the case of experimental data with the application to stroke detection in brains of small animals was done in [43]. We point out that one of the main keys to the success of numerical results of [1, 16, 17] for the reconstruction algorithms of Novikov [37–40] is the use of approximate mathematical models. The same can be said about [28, 41–43]. This concept is similar to the one above.

In section 2, we pose a CIP for a 1D wave-like PDE. In section 3, we study some properties of the Laplace transform of the solution of the forward problem. In section 4, we discuss the concept of the approximate global convergence property. In section 5, we present our numerical method. Convergence analysis can be found in section 6. In section 7, we describe the experimental setup, main uncertainties in the experimental data and the data pre-processing procedure. Imaging results are presented in section 8. Section 9 is devoted to discussion.

2. Statements of forward and inverse problems

Let the function $\varepsilon_r(x)$, $x \in \mathbb{R}$ be the dielectric constant, spatially distributed on the real line. Let the number $d > 1$. We assume below that

$$\varepsilon_r(x) \in [1, d], \quad x \in [0, 1], \quad \varepsilon_r \in C^1(\mathbb{R}), \tag{2.1}$$

$$\varepsilon_r(x) = 1, \quad x \notin (0, 1). \tag{2.2}$$

Thus, the interval $(0, 1)$ is our domain of interest in the inverse problem. The forward problem is

$$\varepsilon_r(x)u_{tt} = u_{xx}, \quad x \in \mathbb{R}, \quad t \in (0, \infty), \tag{2.3}$$

$$u(x, 0) = 0, \quad u_t(x, 0) = \delta(x - x_0), \tag{2.4}$$

$$x_0 = \text{const.} < 0. \tag{2.5}$$

CIP. Determine the coefficient $\varepsilon_r(x)$, *assuming that the following function* $g(t)$ *is known*

$$u(0, t) = g(t), \quad t \in (0, \infty). \tag{2.6}$$

The function $g(t)$ models the backscattering data measured by the Forward Looking Radar. The condition $t \in (0, \infty)$ in (2.6) is not a restrictive one from the numerical standpoint. Indeed, we use the Laplace transform (2.7) to solve this CIP. Since the kernel e^{-st} of this transform decays rapidly with respect to t, then in actuality a finite time interval is sufficient. In addition, the data resulting from the data pre-processing procedure have a finite support in

$(0, \infty)$, see figures 5(a) and (b). Since this is the 1D case, uniqueness theorems for this CIP are well known; see e.g. [35] and references therein.

Consider the Laplace transform

$$w(x, s) = \int_0^\infty u(x, t) \, e^{-st} \, dt := \mathcal{L}u, \quad s \geqslant \underline{s} = \text{const.} > 0, \tag{2.7}$$

where the number $\underline{s} = \underline{s}(\varepsilon_r)$ is sufficiently large. We call the parameter s, *pseudo frequency*. Hence,

$$w_{xx} - s^2 \varepsilon_r(x) w = -\delta(x - x_0), \quad x \in \mathbb{R}, \tag{2.8}$$

$$\lim_{|x| \to \infty} w(x, s) = 0; \tag{2.9}$$

see theorem 3.1 for the proof of (2.9). By (2.6)

$$w(0, s) = \varphi(s) := \mathcal{L}g, s \geqslant \underline{s}. \tag{2.10}$$

We also need to know the derivative $w_x(0, s)$,

$$w_x(0, s) = \rho(s), \quad s \geqslant \underline{s}.$$

Consider the fundamental solution $w_0(x, s)$ of problem (2.8) and (2.9) for $\varepsilon_r(x) \equiv 1$. Then

$$w_0(x, s) = (2s)^{-1} \exp(-s|x - x_0|). \tag{2.11}$$

Denote $\widehat{w}(x, s) = w(x, s) - w_0(x, s)$. Using (2.8)–(2.10), we obtain

$$\widehat{w}_{xx} - s^2 \varepsilon_r(x) \widehat{w} = s^2(\varepsilon_r(x) - 1) w_0, \quad x \in \mathbb{R}, \tag{2.12}$$

$$\lim_{|x| \to \infty} \widehat{w}(x, s) = 0, \tag{2.13}$$

$$\widehat{w}(0, s) = \widehat{\varphi}(s) := \varphi(s) - (2s)^{-1} \exp(-s|x_0|). \tag{2.14}$$

Also, (2.2) and (2.12)–(2.14) imply for $x < 0$,

$$\widehat{w}_{xx} - s^2 \widehat{w} = 0, \quad x < 0, \tag{2.15}$$

$$\lim_{x \to -\infty} \widehat{w}(x, s) = 0, \tag{2.16}$$

$$\widehat{w}(0, s) = \widehat{\varphi}(s). \tag{2.17}$$

It follows from (2.15)–(2.17) that $\widehat{w}(x, s) = \widehat{\varphi}(s) \, e^{sx}$, $x < 0$. Hence, $\widehat{w}_x(0, s) = s\widehat{\varphi}(s) = s(\varphi(s) - (2s)^{-1} \exp(-s|x_0|))$ and thus since $x_0 < 0$, we have

$$w_x(0, s) := \rho(s) = s\varphi(s) - \exp(sx_0). \tag{2.18}$$

3. Some properties of the function $w(x, s)$

Below C^α, $\alpha \in (0, 1)$ are Hölder spaces. In this section, we establish some properties of the function $w = \mathcal{L}u$, which we need for the convergence analysis. Let $f(t)$, $t > 0$ be a piecewise continuous function such that $|f(t)| \leqslant C e^{at}$, $t > 1$, where $C = C(f)$, $a = a(f) = \text{const.} > 0$. Consider two types of Laplace transforms,

$$\mathcal{L}_1(f)(t) = \frac{1}{2\sqrt{\pi} t^{3/2}} \int_0^\infty \tau \exp\left(-\frac{\tau^2}{4t}\right) f(\tau) \, d\tau,$$

$$\mathcal{L}_2(f)(s) = \int_0^\infty f(t) \, e^{-s^2 t} \, dt, \quad s > \sqrt{a(f)}.$$

Lemma 3.1. $\mathcal{L}_2 [\mathcal{L}_1 (f)] (s) = \mathcal{L} (f) (s)$ *for* $s > a(f)$*, where the operator* $\mathcal{L}$ *was defined in (2.7).*

Proof. Using formula (28) of section 4.5 of the book [2], we obtain

$$\int_0^\infty \left[\frac{1}{2\sqrt{\pi} t^{3/2}} \tau \exp\left(-\frac{\tau^2}{4t} \right) \right] e^{-s^2 t} \, dt = e^{-s\tau}, \forall s > 0. \qquad \square$$

Theorem 3.1. *Consider the function* $\varepsilon_r(x) \in C^\alpha (\mathbb{R})$ *satisfying the rest of conditions (2.1) and (2.2). Let (2.5) hold. Then for any number* $s > 0$ *there exists a unique solution* $p(x, s) \in C^{2+\alpha} (|x - x_0| \geqslant \beta) \cap C (\mathbb{R}), \forall \beta > 0$ *of the following problem:*

$$p_{xx} - s^2 \varepsilon_r(x) p = -\delta(x - x_0), \quad x \in \mathbb{R}, \tag{3.1}$$

$$\lim_{|x| \to \infty} p(x, s) = 0. \tag{3.2}$$

Also,

$$0 < p(x, s) \leqslant w_0(x, s), \quad \forall x \in \mathbb{R}. \tag{3.3}$$

In addition, let $|x - x_0| \geqslant \beta = \text{const.} > 0$*. Then there exists a sufficiently large number* $\widehat{s} = \widehat{s}(d, \beta)$ *such that*

$$p(x, s) > w_d(x, s), \quad \forall x \in [x_0 + \beta, \infty), \quad \forall s \geqslant \widehat{s}, \tag{3.4}$$

where $w_d(x, s)$ *is the fundamental solution of equation (2.8) for the case* $\varepsilon_r(x) \equiv d$*,*

$$w_d(x, s) = (2s)^{-1} \exp(-s\sqrt{d}|x - x_0|). \tag{3.5}$$

Finally, there exists a sufficiently large number $\underline{s} = \underline{s}(\varepsilon_r) > 0$ *such that*

$$w(x, s) := \mathcal{L}(u)(x, s) = p(x, s), \quad \forall s \geqslant \underline{s}(\varepsilon_r), \quad \forall x \in \mathbb{R}. \tag{3.6}$$

Thus, (3.2) implies that (2.9) holds for $s \geqslant \underline{s} = \underline{s}(\varepsilon_r)$*.*

Proof. Let the function $v(x, t)$ be the solution of the following Cauchy problem:

$$\varepsilon_r(x) v_t = v_{xx}, \quad (x, t) \in \mathbb{R} \times (0, \infty), \tag{3.7}$$

$$v(x, 0) = \delta(x - x_0). \tag{3.8}$$

Let the function $v_0(x, t)$ be the solution of problem (3.7), (3.8) for the case $\varepsilon_r(x) \equiv 1$,

$$v_0(x, t) = \frac{1}{2\sqrt{\pi t}} \exp\left[-\frac{(x - x_0)^2}{4t} \right].$$

Let $\widehat{v}(x, t) = v(x, t) - v_0(x, t)$. Then

$$\widehat{v}_{xx} - \varepsilon_r(x) \widehat{v}_t = (\varepsilon_r(x) - 1) v_{0t}, \quad \widehat{v}(x, 0) = 0. \tag{3.9}$$

Detailed estimates of the fundamental solution of a general parabolic equation in [32, chapter 4] imply that $\widehat{v} \in C^{2+\alpha, 1+\alpha/2} (\mathbb{R} \times [0, T]), \forall T > 0$. Denote

$$\widetilde{v}(x, t) = \int_0^t \widehat{v}(x, \tau) \, d\tau = \int_0^t (v - v_0)(x, \tau) \, d\tau. \tag{3.10}$$

By (3.9)

$$\widetilde{v}_{xx} - \varepsilon_r(x) \widetilde{v}_t = (\varepsilon_r(x) - 1) v_0, \widetilde{v}(x, 0) = 0. \tag{3.11}$$

By (2.2) and (2.5), $\varepsilon_r(x) - 1 = 0$ in a neighborhood of the source point $\{x_0\}$. Hence, applying (2.2), we obtain $(\varepsilon_r(x) - 1)\, v_0(x, t) \geqslant 0$ in $\mathbb{R} \times [0, \infty)$. Hence, applying the maximum principle of [23, theorem 1 of chapter 2] to (3.11) we obtain

$$\widetilde{v}(x, t) \leqslant 0 \quad \text{in} \quad \mathbb{R} \times [0, \infty). \tag{3.12}$$

On the other hand, theorem 11 of chapter 2 of [23] ensures that the fundamental solution of the parabolic equation is positive for $t > 0$. Hence,

$$v(x, t) > 0, \quad t > 0. \tag{3.13}$$

Hence, (3.10), (3.12) and (3.13) imply that

$$0 < \int_0^t v(x, \tau)\, \mathrm{d}\tau \leqslant \int_0^t v_0(x, \tau)\, \mathrm{d}\tau. \tag{3.14}$$

Using the Fubini theorem, formula (27) of section 4.5 of the book [2] and (2.11), we obtain

$$\mathcal{L}_2\left(\int_0^t v_0(x, \tau)\, \mathrm{d}\tau\right) = \frac{1}{s^2}\mathcal{L}_2(v_0) = \frac{w_0(x, s)}{s^2}. \tag{3.15}$$

Hence, using (3.13) and (3.14) and Fubini theorem, we obtain

$$\mathcal{L}_2\left(\int_0^t v(x, \tau)\, \mathrm{d}\tau\right) = \frac{1}{s^2}\mathcal{L}_2(v)(x, s) := \frac{y(x, s)}{s^2} \leqslant \frac{w_0(x, s)}{s^2}, \tag{3.16}$$

By (2.11), (3.13) and (3.16)

$$\lim_{|x| \to \infty} y(x, s) = 0. \tag{3.17}$$

Next, by (3.10) and (3.11) $\widetilde{v}_{xx} = \varepsilon_r(x)v - v_0$. Hence, $|\widetilde{v}_{xx}| \leqslant dv + v_0$. Therefore,

$$\int_0^\infty |\widetilde{v}_{xx}(x, t)|\, \mathrm{e}^{-s^2 t}\, \mathrm{d}t < \infty.$$

Hence,

$$\partial_x^2 \int_0^\infty \widetilde{v}(x, t)\, \mathrm{e}^{-s^2 t}\, \mathrm{d}t = \int_0^\infty \widetilde{v}_{xx}(x, t)\, \mathrm{e}^{-s^2 t}\, \mathrm{d}t = \varepsilon_r(x)y - w_0. \tag{3.18}$$

On the other hand,

$$\int_0^\infty \widetilde{v}_{xx}(x, t)\, \mathrm{e}^{-s^2 t}\, \mathrm{d}t = \int_0^\infty \left(\int_0^t v_{xx}(x, \tau)\, \mathrm{d}\tau\right) \mathrm{e}^{-s^2 t}\, \mathrm{d}t - \int_0^\infty \left(\int_0^t v_{0xx}(x, \tau)\, \mathrm{d}\tau\right) \mathrm{e}^{-s^2 t}\, \mathrm{d}t$$

$$= s^{-2}\left(y_{xx} - w_{0xx}\right).$$

Comparing this with (3.18) and keeping in mind that $w_{0xx} - s^2 w_0 = -\delta(x - x_0)$, we obtain

$$y_{xx} - s^2 \varepsilon_r(x)y = -\delta(x - x_0). \tag{3.19}$$

By (3.17) and (3.19), the function $y(x, s) = \mathcal{L}_2(v)(x, s)$ satisfies conditions (3.1) and (3.2). It follows from above that $y(x, s) \in C^{2+\alpha}(|x - x_0| \geqslant \beta) \cap C(\mathbb{R})$, $\forall \beta, s > 0$. Uniqueness of the solution of problem (3.1) and (3.2) for this class of functions can be easily proven in the standard way using the maximum principle for elliptic equations and (3.2). Hence, problem (3.1) and (3.2) have the unique solution $p(x, s) := y(x, s) \in C^{2+\alpha}(|x - x_0| \geqslant \beta) \cap C(\mathbb{R})$, $\forall \beta, s > 0$. The right estimate (3.3) follows from (3.16), and the left estimate follows from (3.16). Lemma 3.1 implies (3.6).

We now prove (3.4). We obtain from (2.2), (3.1) and (3.2):

$$p(x, s) = \frac{\exp(-s|x - x_0|)}{2s} - \frac{s}{2}\int_0^1 \exp(-s|x - \xi|)(\varepsilon_r(\xi) - 1)\, p(\xi, s)\, \mathrm{d}\xi. \tag{3.20}$$

Hence, by (2.1) and the right inequality (3.3)

$$p(x, s) \geqslant \frac{\exp(-s|x - x_0|)}{2s} - \frac{(d-1)}{4} \int_0^1 \exp(-s|x - \xi|) \exp(-s|\xi - x_0|) \, d\xi.$$

Assume now that $x \in (x_0, 0)$. Then,

$$p(x, s) \geqslant \frac{\exp[-s(x - x_0)]}{2s} - \frac{(d-1)\exp[s(x + x_0)]}{4} \int_0^1 e^{-2s\xi} \, d\xi$$

$$= \frac{\exp[-s(x - x_0)]}{2s} \left[1 - \frac{(d-1)(1 - e^{-2s}) e^{2sx}}{4} \right].$$

Therefore,

$$\frac{p(x, s)}{w_d(x, s)} \geqslant \exp[s(\sqrt{d} - 1)(x - x_0)] \left[1 - \frac{(d-1)(1 - e^{-2s}) e^{2sx}}{4} \right], \quad \forall x \in (x_0, 0).$$

Hence, if $\beta = \text{const.} \in (0, |x_0|)$, then there exists a number $\widehat{s} = \widehat{s}(d, \beta)$ such that

$$\frac{p(x, s)}{w_d(x, s)} > 1, \quad \forall s \geqslant \widehat{s} = \widehat{s}(d, \beta), \quad \forall x \in \left[x_0 + \frac{\beta}{2}, x_0 + \beta \right]. \tag{3.21}$$

Consider now the difference $\widetilde{p}(x, s) = p(x, s) - w_d(x, s)$. Then,

$$\widetilde{p}_{xx} - s^2 \varepsilon_r(x) \widetilde{p} = s^2 (\varepsilon_r(x) - d) w_d < 0, \quad x \in [x_0 + \beta, \infty), \tag{3.22}$$

$$\lim_{x \to \infty} \widetilde{p}(x, s) = 0. \tag{3.23}$$

Let $a > x_0 + \beta$ be an arbitrary number. Consider the function $\widetilde{p}(x, s)$ on the interval $[x_0 + \beta, a]$ for $s \geqslant \widehat{s}(d, \beta)$. Then, the maximum principle for elliptic equations (3.21) and (3.22) implies that the negative minimum of $\widetilde{p}(x, s)$ on this interval can be achieved only at $x = a$. Setting $a \to \infty$ and using (3.23), we obtain that $\widetilde{p}(x, s) \geqslant 0$ for $x \in [x_0 + \beta, \infty), s \geqslant \widehat{s}(d, \beta)$.

Assume now that there exist a point $\bar{x} \in [x_0 + \beta, \infty)$ and a number $s \geqslant \widehat{s}(d, \beta)$ such that $\widetilde{p}(\bar{x}, s) = 0$. Since $\widetilde{p}(x, s) \geqslant 0$ for $x \in [x_0 + \beta, \infty)$, therefore,

$$\widetilde{p}(\bar{x}, s) = 0 = \min_{[x_0 + \beta, \infty)} \widetilde{p}(x, s). \tag{3.24}$$

Hence, $\widetilde{p}_{xx}(\bar{x}, s) \geqslant 0$. However, this and (3.24) contradict to the inequality in (3.22). $\qquad \square$

Corollary 3.1. *Let the function $\varepsilon_r(x) \in C^\alpha(\mathbb{R})$ satisfy the rest of conditions (2.1) and (2.2). For each $s > 0$ and for each $x \in \mathbb{R}$, the integral of the Laplace transform $\mathcal{L}_2(v(x, t))$ converges absolutely.*

Proof. See (3.14), (3.15) and (3.16). $\qquad \square$

Remark 3.1. By (3.6) the function $\varphi(s)$ in (2.10) is defined only for $s \geqslant \underline{s}(\varepsilon_r)$. However, using lemma 3.1 and corollary 3.1, we set below $\varphi(s) := \mathcal{L}_2[\mathcal{L}_1(g)](s), \forall s > 0$, where the function $g(t)$ is defined in (2.6).

Theorem 3.2. *Let the function $\varepsilon_r(x) \in C^\alpha(\mathbb{R})$ satisfy the rest of conditions (2.1), (2.2) and (2.5). Let the number $\bar{s} \geqslant \widehat{s}(|x_0|, d)$, where the number $\widehat{s}$ was defined in theorem 3.1. Let the function $p(x, \bar{s}; \varepsilon_r) := p(x, \bar{s}) \in C^{2+\alpha}(|x - x_0| \geqslant \beta) \cap C(\mathbb{R}), \forall \beta > 0$ be the solution of the problem (3.1) and (3.2). Denote*

$$f_k(x, \bar{s}; \varepsilon_r) = \bar{s}^{-2} \partial_x^k [\ln p(x, \bar{s})], \quad k = 1, 2.$$

Then, there exists a constant $B = B(x_0, d, \overline{s}) > 1$ such that for all such functions ε_r,

$$\|f_k(x, \overline{s}; \varepsilon_r)\|_{C[0,1]} \leqslant B, \quad k = 1, 2. \tag{3.25}$$

Also, for any two functions $\varepsilon_r^{(1)}$ and $\varepsilon_r^{(2)}$ satisfying conditions of this theorem

$$\left\|f_k\left(x, \overline{s}; \varepsilon_r^{(1)}\right) - f_k\left(x, \overline{s}; \varepsilon_r^{(2)}\right)\right\|_{L_2(0,1)} \leqslant B\left\|\varepsilon_r^{(1)} - \varepsilon_r^{(2)}\right\|_{L_2(0,1)}, \quad k = 1, 2. \tag{3.26}$$

Proof. In this proof $B = B(x_0, d, \overline{s}) > 1$ denotes different constants depending on the listed parameters. We have

$$f_1 = \frac{p_x}{\overline{s}^2 p}, \quad f_2 = \frac{p_{xx}}{\overline{s}^2 p} - \frac{p_x^2}{\overline{s}^2 p^2}. \tag{3.27}$$

Hence, by (3.4)

$$|f_1(x, \overline{s}; \varepsilon_r)| \leqslant B|p_x(x, \overline{s}; \varepsilon_r)|, \quad |f_2(x, \overline{s}; \varepsilon_r)| \leqslant B[|p_{xx}| + |p_x|^2](x, \overline{s}; \varepsilon_r), \quad x \in [0, 1]. \tag{3.28}$$

To estimate the function $|p_x|$, we use the integral equation (3.20). We have for $x \in (0, 1)$,

$$p_x(x, s) = -\frac{\exp[-s(x - x_0)]}{2} + \frac{s^2}{2}\int_0^1 \operatorname{sgn}(x - \xi)\exp(-s|x - \xi|)(\varepsilon_r(\xi) - 1)p(\xi, s)\,\mathrm{d}\xi.$$

Hence, (2.1) and (3.3) imply that $|p_x| \leqslant B$ for $x \in [0, 1]$. Since $\delta(x - x_0) = 0$ for $x \in [0, 1]$, (3.3) implies that $p_{xx} = s^2\varepsilon_r(x)p$ for $x \in [0, 1]$. Hence, by (2.1) and (3.3) $|p_{xx}| \leqslant B, x \in [0, 1]$. Thus, (3.28) implies (3.25).

We now prove (3.26). Let $\widetilde{p}(x, s) = p\left(x, \overline{s}; \varepsilon_r^{(1)}\right) - p\left(x, \overline{s}; \varepsilon_r^{(2)}\right)$. Then by (3.1)

$$\widetilde{p}_{xx} - \overline{s}^2\varepsilon_r^{(1)}(x)\widetilde{p} = \overline{s}^2\left(\varepsilon_r^{(1)} - \varepsilon_r^{(2)}\right)(x)p\left(x, \overline{s}; \varepsilon_r^{(1)}\right), \quad x \in \mathbb{R}. \tag{3.29}$$

In addition, it follows from (3.3) and (3.20) that functions $\partial_x^j\widetilde{p}(x, \overline{s})$, $j = 0, 1$ and 2 decay exponentially with $|x| \to \infty$. Hence, multiplying (3.29) by $\widetilde{p}$, integrating over $\mathbb{R}$ and using (2.1) and (3.3), we obtain $\|\widetilde{p}\|_{H^1(\mathbb{R})} \leqslant B\left\|\varepsilon_r^{(1)} - \varepsilon_r^{(2)}\right\|_{L_2(0,1)}$. Hence, (3.25) and (3.29) lead to

$$\|\widetilde{p}\|_{H^2(0,1)} \leqslant B\left\|\varepsilon_r^{(1)} - \varepsilon_r^{(2)}\right\|_{L_2(0,1)}.$$

Thus, (3.4) and (3.27) imply (3.26). □

4. Approximate global convergence

4.1. The concept

As to the 1D version of the technique, which was published in [30] and which is used here, originally the work of [30] was considered 'only as a preliminary step before applying similar ideas to 2D and 3D cases' [30, p 125]. The authors of [30] meant the incorporation of the quasi-reversibility method (QRM) in the techniques of [5–12, 26, 27, 31, 47]; see section 5.

Least-squares functionals for MCIPs with single measurement data suffer from multiple local minima and ravines. This implies the local convergence of conventional numerical methods for those MCIPs. The latter mean that iterations should start from a point located in a sufficiently small neighborhood of the exact solution. The central question addressed in the publications above was: *How does one construct an effective numerical method, which would lead to a point in a sufficiently small neighborhood of the exact solution of an MCIP without any a priori information about that neighborhood with a rigorous guarantee of reaching that neighborhood*?

Because of the enormous challenge of addressing this central question (section 1), the approach of [5–12, 26, 27, 30, 31, 47], as well as that of the current paper, consist of the following six steps.

Step 1. A reasonable approximate mathematical model is proposed. The accuracy of this model cannot be rigorously estimated.

Step 2. A numerical method is developed, which works within the framework of this model.

Step 3. A theorem is proven, which guarantees that, within the framework of this model, the numerical method of step 2 indeed reaches a sufficiently small neighborhood of the exact solution, as long as the errors both in the data and in some additional approximations are sufficiently small. It is *central* to our approach that this theorem should not rely either on the assumption about a knowledge of any point in a small neighborhood of the exact solution or on the assumption of knowledge of the background medium inside of the domain of interest.

Step 4. That numerical method is tested on computationally simulated data.

Step 5. (Optional). The numerical method of step 2 is tested on experimental data. To have a truly unbiased case, blind data are preferable. This step is optional because it is usually not easy to actually obtain experimental data.

Step 6. Finally, if the results of step 4 and (optionally) step 5 are good ones, then that approximate mathematical model is proclaimed as a valid one.

Step 6 is logical because its condition is that the resulting numerical method is proved to be effective, i.e. goal 2 is successfully met; see also remark 4.4. After a finite (rather than infinite) number of iterations it is sufficient to achieve the small neighborhood of the exact solution. Next, because of approximations in the mathematical model, the resulting solution can be refined via a locally convergent numerical method. The latter led to a two-stage numerical procedure in [6–12, 31, 47]. In the first stage, the numerical method of step 2 is applied. In the second stage, the adaptive finite element method (adaptivity) for MCIPs takes the solution of the first stage as the starting point for iterations and refines it.

4.2. Definition

Considerations of subsection 4.1 led to the introduction of the approximate global convergence property in [6, 12]. Since this definition is new, it is worth repeating it here. Recall that one of the backbone principles of the theory of ill-posed problems is that, given an ill-posed problem, it is reasonable to assume uniqueness and existence of the exact solution of this problem for the 'ideal' noiseless data [6, 22, 46]. It is not necessary for an algorithm addressing the above central question to start from any such point. In fact, it is sufficient for it to start from such a reasonable point, which would not contain information about a small neighborhood of the exact solution. The question of the validity of the approximate mathematical model M of definition 4.1 should be addressed in steps 4 and 5 of subsection 4.1.

Definition 4.1. (Approximate global convergence) [6, 12]. *Consider a nonlinear ill-posed problem P. Suppose that this problem has a unique solution $x^* \in B$ for the noiseless data y^*, where B is a Banach space with the norm $\|\cdot\|_B$. We call x^* the 'exact solution' or the 'correct solution'. Suppose that a certain approximate mathematical model M is proposed to solve the problem P numerically. Assume that, within the framework of the model M, this problem has a unique exact solution x_M^* and let $x_M^* = x^*$. Consider an iterative numerical method for solving the problem P. Suppose that this method produces a sequence of points $\{x_n\}_{n=1}^N \subset B$, where $N \in [1, \infty)$. Let a sufficiently small number $\theta \in (0, 1)$. We call this numerical method approximately globally convergent of the level θ, or shortly globally convergent if, within the framework of the approximate model M, a theorem is proven, which guarantees that, without any*

a priori knowledge of a sufficiently small neighborhood of x^*, there exists a number $\overline{N} \in [1, N)$ such that

$$\|x_n - x^*\|_B \leqslant \theta, \quad \forall n \geqslant \overline{N}. \tag{4.1}$$

Suppose that iterations are stopped at a certain number $k \geqslant \overline{N}$. Then, the point x_k is denoted $x_k := x_{\text{glob}}$ and is called 'the approximate solution resulting from this method'.

Remark 4.1. We repeat that we have introduced this definition because, in simple terms, nothing else works for MCIPs with single measurement data; see comments about goals 1 and 2 in section 1.

Remark 4.2. The most important requirement of definition 4.1 is that this numerical method should provide a sufficiently good approximation for the exact solution x^* without any *a priori* knowledge of a sufficiently small neighborhood of x^*. Furthermore, one should have a rigorous guarantee of the latter within the framework of the model M. In other words, step 1 of subsection 4.1 should be addressed.

Remark 4.3. Unlike the classical convergence, this definition does not require $\lim_{n \to \infty} x_n = x^*$. Furthermore, the total number N of iterations can be finite.

Remark 4.4. As to the use of the approximate mathematical model M, all equations of mathematical physics are approximate ones. The main criterion of their validity is the accuracy of descriptions of experimental data, which is exactly what we do. Also, it is well known that the Huygens–Fresnel optics is not yet rigorously derived from the Maxwell equations; see section 8.1 of the classical book of Born and Wolf [14]. Nevertheless, it is the Huygens–Fresnel theory which describes the experimental data of the diffraction optics very well. Furthermore, the entire optical industry nowadays is based on the Huygens–Fresnel theory. On the other hand, the derivation of this theory from the Maxwell equations is based on some non-rigorous approximations. Analogously, although the numerical method of [5–12, 26, 27, 31, 47] is based on an approximate model, goal 2 has been consistently achieved.

5. Numerical method

Although a detailed description of the numerical method of this section can be found in [30], we still present it rather briefly here in order to refer to some formulas in the convergence analysis in section 6. Also, because of (2.2), we consider here the function $\ln(w/w_0)$ instead of $\ln w(x, s)$ in [30]. Let $w(x, s) \in C^{2+\alpha} (|x - x_0| \geqslant \beta) \cap C(\mathbb{R}), \forall \beta, s > 0$ be the solution of problem (2.8) and (2.9); see theorem 3.1.

5.1. Integral differential equation

Since by (3.3) $w(x, s) > 0$, we can consider the function $r(x, s)$,

$$r(x, s) = s^{-2} [\ln w(x, s) - \ln w_0(x, s)] = s^{-2} \ln [(w/w_0)(x, s)].$$

Then, (2.8), (2.10) and (2.18) imply that

$$r_{xx} + s^2 r_x^2 - 2sr_x = \varepsilon_r(x) - 1, \quad x > 0, \tag{5.1}$$

$$r(0, s) = \varphi_0(s), \quad r_x(0, s) = \varphi_1(s), \tag{5.2}$$

$$\varphi_0(s) = s^{-2} [\ln \varphi(s) - \ln(2s)] + x_0 s^{-1}, \quad \varphi_1(s) = 2/s - \exp(sx_0)(s^2 \varphi(s))^{-1}. \tag{5.3}$$

By (2.2), (2.5), (2.8) and (2.9), $w(x, s) = C(s)\,\mathrm{e}^{-sx}$ for $x \geqslant 1$, where $C(s)$ is a certain function s dependent on s. Hence,

$$r_x(1, s) = 0. \tag{5.4}$$

Differentiate equation (5.1) with respect to s. Then,

$$q(x, s) = \partial_s r(x, s), \quad \psi_0(s) = \varphi_0'(s), \quad \psi_1(s) = \varphi_1'(s), \tag{5.5}$$

$$r(x, s) = -\int_s^{\bar{s}} q(x, \tau)\,\mathrm{d}\tau + V(x, \bar{s}), \tag{5.6}$$

$$V(x, \bar{s}) = \bar{s}^{-2}[\ln w(x, \bar{s}) - \ln w_0(x, \bar{s})] = r(x, \bar{s}). \tag{5.7}$$

Here, $\bar{s} > 0$ is a sufficiently large number which is chosen in numerical experiments. We call $V(x, \bar{s})$ the *tail function*. Actually, $\bar{s}$ is the regularization parameter of this method. Using (5.1)–(5.7), we obtain

$$q_{xx} - 2s^2 q_x \int_s^{\bar{s}} q_x(x, \tau)\,\mathrm{d}\tau + 2s\left[\int_s^{\bar{s}} q_x(x, \tau)\,\mathrm{d}\tau\right]^2 - 2s q_x + 2\int_s^{\bar{s}} q_x(x, \tau)\,\mathrm{d}\tau$$

$$+ 2s^2 q_x V_x - 4s V_x \int_s^{\bar{s}} q_x(x, \tau)\,\mathrm{d}\tau + 2s(V_x)^2 - 2V_x = 0, \quad s \in [\underline{s}, \bar{s}], \tag{5.8}$$

$$q(0, s) = \psi_0(s), \quad q_x(0, s) = \psi_1(s), \quad q_x(1, s) = 0, \quad s \in [\underline{s}, \bar{s}]. \tag{5.9}$$

Lemma 2.1 of [30] implies for $k = 0, 1$ and 2

$$D_x^k r(x, s) = D_x^k\left\{-\frac{1}{s}\left[\int_{x_0}^x \sqrt{\varepsilon_r(\xi)}\,\mathrm{d}\xi - (x - x_0)\right] + O\left(\frac{1}{s^3}\right)\right\}, \quad x > 0, \quad s \to \infty. \tag{5.10}$$

Hence, the function $V(x, \bar{s}) = r(x, \bar{s})$ is small for large values of $\bar{s}$,

$$\|V(x, \bar{s})\|_{C^2[0,1]} = O(1/\bar{s}). \tag{5.11}$$

The main difficulty of this numerical method is in the solution of problem (5.8) and (5.9). Equation (5.8) has two unknown functions q and V. To approximate both of them, we use a predictor/corrector-like scheme. First, given an approximation for V, we update q via equation (5.8) and (5.9). Next, we update the unknown coefficient $\varepsilon_r(x)$ and solve the forward problem (2.8) and (2.9) for $s := \bar{s}$ with this updated coefficient $\varepsilon_r(x)$. This is our predictor-like step. On the corrector-like step we update the tail function $V(x, \bar{s})$ via (5.7).

Consider a partition of the interval $[\underline{s}, \bar{s}]$ into N small subintervals with the grid step size $h > 0$ and assume that the function $q(x, s)$ is piecewise constant with respect to s,

$$\underline{s} = s_N < s_{N-1} < \cdots < s_0 = \bar{s}, s_{i-1} - s_i = h; \quad q(x, s) = q_n(x), \text{ for } s \in (s_n, s_{n-1}). \tag{5.12}$$

Let $\mu \gg 1$ be a large parameter which should be chosen in numerical experiments. Multiply both sides of equation (5.8) by the Carleman weight function (CWF),

$$\mathcal{C}_{n,\mu}(s) = \exp[-\mu(s_{n-1} - s)], \quad s \in (s_n, s_{n-1}), \tag{5.13}$$

and integrate with respect to $s \in (s_n, s_{n-1})$. The CWF is introduced in order to mitigate the influence of the nonlinear term $B_n(\mu, h)\left(q_n'\right)^2$ in the resulting equation. If h is fixed, then

$$B_n(\mu, h) = O(\mu^{-1}), \quad \mu \to \infty. \tag{5.14}$$

We ignore the nonlinear term, since we observed in our computations that it provides only an insignificant impact in results for $\mu \geqslant 50$. For each n, we perform inner iterations with

respect to the tail function. This way we obtain functions $q_{n,k}$ and $V_{n,k}$. The equation for the pair $(q_{n,k}, V_{n,k})$ is

$$
q_{n,k}'' - \left(A_{1,n} h \sum_{j=0}^{n-1} q_j' - A_{1,n} V_{n,k}' - 2A_{2,n} \right) q_{n,k}' = -A_{2,n} h^2 \left(\sum_{j=0}^{n-1} q_j' \right)^2 + 2h \sum_{j=0}^{n-1} q_j'
$$

$$
+ 2A_{2,n} V_{n,k}' \left(h \sum_{j=0}^{n-1} q_j' \right) - A_{2,n} \left(V_{n,k}' \right)^2 + 2A_{2,n} V_{n,k}', \quad q_0 :\equiv 0, \quad x \in (0, 1),
$$

$$
\tag{5.15}
$$

$$
q_{n,k}(0) = \psi_{0,n}, \quad q_{n,k}'(0) = \psi_{1,n}, \quad q_{n,k}'(1) = 0, \tag{5.16}
$$

$$
\psi_{0,n} = \frac{1}{h} \int_{s_n}^{s_{n-1}} \psi_0(s)\, ds, \quad \psi_{1,n} = \frac{1}{h} \int_{s_n}^{s_{n-1}} \psi_1(s)\, ds. \tag{5.17}
$$

Here, $A_{1,n}$ and $A_{2,n}$ are certain numbers, whose exact expression is given in [5, 6]. It is known that

$$
\max_{\mu h \geqslant 1} (A_{1,n}, A_{2,n}) \leqslant 8\overline{s}^2. \tag{5.18}
$$

Boundary conditions (5.16) for equation (5.15) are overdetermined ones. On the other hand, the QRM is well suitable for solutions of such problems. Hence, we use the QRM to approximate functions $q_{n,k}$; see subsection 5.3 and remark 5.1.

5.2. The iterative process

Since equations (5.15) are generated by the Volterra-like integral differential equation (5.8), it is natural to solve them sequentially starting from $n = 1$. Let $\xi \in (0, 1)$ be a sufficiently small number. Consider a function $\chi(x) \in C^2(\mathbb{R})$ such that

$$
\chi(x) = \begin{cases} 1, & x \in (\xi, 1 - \xi), \\ \text{between 0 and 1} & \text{for } x \in (0, \xi) \cup (1 - \xi, 1), \\ 0, & x \in \mathbb{R} \setminus (0, 1). \end{cases} \tag{5.19}
$$

The existence of such functions is well known from the real analysis course. We choose the first guess for the tail function $V_0(x)$ as in subsection 6.2. For each $n \in [1, N]$, we perform m iterations with respect to tails. Hence, we obtain three finite sequences of functions:

$$
\{q_{n,k}(x)\}_{(n,k)=(1,1)}^{(N,m)}, \quad \{V_{n,k}(x)\}_{(n,k)=(1,1)}^{(N,m)}, \quad \left\{\varepsilon_r^{(n,k)}(x)\right\}_{(n,k)=(1,1)}^{(N,m)}, \quad x \in [0, 1]. \tag{5.20}
$$

Step $n^{(1)}$, $n \in [1, N]$. Suppose that functions $q_j(x) \in H^4(0, 1)$ and $V_{n-1}(x) \in C^3[0, 1]$ are constructed. We set $V_{n,1}(x) := V_{n-1}(x)$. In particular, $V_{1,1}(x) := V_0(x)$. Next, using the QRM (subsection 5.3), we approximately solve equation (5.15) for $k = 1$ with overdetermined boundary conditions (5.16) and find the function $q_{n,1} \in H^4(0, 1)$ this way (remark 5.1). Hence, by the embedding theorem $q_{n,1} \in C^3[0, 1]$. Next, we find the approximation $\varepsilon_r^{(n,1)}$ for the unknown coefficient $\varepsilon_r(x)$ via the following two formulas:

$$
r_{n,1}(x) = -hq_{n,1} - h \sum_{j=0}^{n-1} q_j + V_{n,1}, \quad x \in [0, 1], \tag{5.21}
$$

$$
\overline{\varepsilon}_r^{(n,1)}(x) = 1 + r_{n,1}''(x) + s_n^2 \left[r_{n,1}'(x) \right]^2 - 2s_n r_{n,1}'(x), \quad x \in [0, 1], \tag{5.22}
$$

$$
\varepsilon_r^{(n,1)}(x) = \begin{cases} \overline{\varepsilon}_r^{(n,1)}(x), & \text{if } \overline{\varepsilon}_r^{(n,1)}(x) \in [1, d], x \in [0, 1], \\ 1, & \text{if } \overline{\varepsilon}_r^{(n,1)}(x) < 1, x \in [0, 1], \\ d, & \text{if } \overline{\varepsilon}_r^{(n,1)}(x) > d, x \in [0, 1]. \end{cases} \tag{5.23}
$$

Hence, $\overline{\varepsilon}_r^{(n,1)} \in C^1 [0, 1]$ and $\varepsilon_r^{(n,1)} \in C^\alpha [0, 1]$, $\forall \alpha \in (0, 1)$. Formulas (5.21) and (5.22) are obvious discrete analogues of formulas (5.1) and (5.6), respectively. Consider the function

$$\widehat{\varepsilon}_r^{(n,1)}(x) = (1 - \chi(x)) + \chi(x)\varepsilon_r^{(n,1)}(x), \quad x \in \mathbb{R}. \tag{5.24}$$

It can be easily proven that $\widehat{\varepsilon}_r^{(n,1)}(x) \in [1, d]$ for $x \in \mathbb{R}$ This implies the ellipticity of the operator (2.8) for

$$\varepsilon_r(x) := \widehat{\varepsilon}_r^{(n,1)}(x) \in C^\alpha(\mathbb{R}). \tag{5.25}$$

Hence, we solve the forward problem (2.8), (2.9) and (5.25) for $s := \overline{s}$. Let $w_{n,1}(x, \overline{s})$ be the solution of this problem considered in theorem 3.1. Then, using (5.7), we set for the next tail

$$V_{n,2}(x) := \frac{\ln w_{n,1}(x, \overline{s}) - \ln w_0(x, \overline{s})}{\overline{s}^2}. \tag{5.26}$$

Step $n^{(k)}, n \in [1, N], k \in [2, m]$. Suppose that functions $q_j(x) \in H^4(0, 1)$ and $j \in [0, n-1]$, $V_{n,k}(x) \in C^{2+\alpha}[0, 1]$ are constructed. Using the QRM, we approximately solve the problem (5.15) and (5.16). This gives us the function $q_{n,k} \in H^4(0, 1) \subset C^3[0, 1]$. Next, we find the approximation $\varepsilon_r^{(n,k)} \in C^\alpha[0, 1]$ for the function $\varepsilon_r(x)$, using formulas (5.21)–(5.23), where the index '1' is replaced with the index 'k'. Suppose now that $n < N$. Then, we construct the function $\widehat{\varepsilon}_r^{(n,k)}(x)$ via (5.24), where $(n, 1)$ is replaced with (n, k) and solve the forward problem (2.8) and (2.9) with $\varepsilon_r(x) := \widehat{\varepsilon}_r^{(n,k)}(x)$ and $s := \overline{s}$. If $k < m$, then calculate the new tail $V_{n,k+1}(x)$ by formula (5.26) where indices $(n, 1)$ and $(n, 2)$ are replaced with (n, k) and $(n, k+1)$, respectively. If, however, $n < N$ and $k = m$, then we set

$$V_n(x) := V_{n,m+1}(x) \in C^3[0, 1], \quad q_n(x) := q_{n,m}(x) \tag{5.27}$$

and go to the step $(n+1)^{(1)}$. Let $n = N$ and $k = m$. Hence, sequences (5.20) are constructed. Then, we set $\varepsilon_{r,\text{glob}}(x) := \varepsilon_r^{(N,m)} \in C^\alpha[0, 1]$ and stop iterations. The function $\varepsilon_{r,\text{glob}}(x)$ is our final solution as defined in definition 4.1.

5.3. The quasi-reversibility method (QRM)

The QRM was first proposed in [33]. We refer to, e.g., [15, 18, 29] and references cited there for some further developments. The QRM can solve linear ill-posed boundary value problems for many PDEs, including problems with overdetermined boundary conditions. It finds least-squares solutions. Let

$$a_{n,k}(x) = A_{1,n}h \sum_{j=0}^{n-1} q_j' - A_{1,n}V_{n,k}' - 2A_{2,n},$$

and $H_{n,k}(x)$ be the right-hand side of equation (5.15). Then $a_{n,k} \in C^2[0, 1]$, $H_{n,k} \in L_2(0, 1)$. Equation (5.15) can be rewritten as

$$L_{n,k}(q_{n,k}) := q_{n,k}'' - a_{n,k}q_{n,k}' = H_{n,k}.$$

Let $\gamma \in (0, 1)$ be the regularization parameter. In the QRM, we minimize the following Tikhonov functional with respect to the function $q_{n,k}$, subject to the boundary conditions (5.16),

$$J_\gamma(q_{n,k}, H_{n,k}) = \|L_{n,k}(q_{n,k}) - H_{n,k}\|_{L_2(0,1)}^2 + \gamma \|q_{n,k}\|_{H^4(0,1)}^2. \tag{5.28}$$

Remark 5.1. There is a peculiarity of this technique in the 1D case. We use the approximate least-squares QRM solutions of problem (5.15) and (5.16). On the other hand, it seems to be at the first glance that for a given function $V_{n,k}$ one can find the function $q_{n,k}$ via solving equation (5.15) with only two out of three boundary conditions in (5.16). However, our attempt to do so for computationally simulated data has failed to produce good quality results; see remark 3.1 on page 130 of [30]. This is because of the approximate nature of our mathematical model.

Lemma 5.1 (Carleman estimate, see [29, p 168] and [30]). *For any function* $u \in H^2(0, 1)$ *with* $u(0) = u'(0) = 0$ *and for any parameter* $\lambda \geqslant 1$, *the following Carleman estimate holds:*

$$\int_0^1 (u'')^2 \, \mathrm{e}^{-2\lambda x} \, \mathrm{d}x \geqslant \frac{1}{16} \int_0^1 [8(u'')^2 + \lambda (u')^2 + \lambda^3 (u)^2] \mathrm{e}^{-2\lambda x} \, \mathrm{d}x. \tag{5.29}$$

Lemma 5.2 [30]. *For any number* $\gamma \in (0, 1)$ *and for each function* $F \in L_2(0, 1)$, *there exists a unique minimizer* $u_\gamma \in H^4(0, 1)$ *with* $u_\gamma(0) = u'_\gamma(0) = 0$ *of the functional* $J_\gamma(u, F)$ *in (5.28) and*

$$\|u_\gamma\|_{H^4(0,1)} \leqslant C \gamma^{-1/2} \|F\|_{L_2(0,1)},$$

where the constant $C > 0$ *is independent of* $a_{n,k}, F, u_\gamma, \gamma$. *Let* $\|a_{n,k}\|_{C[0,1]} \leqslant a_0$, *where* $a_0 = \mathrm{const.} > 0$, *Let the function* $u \in H^4(0, 1)$, $L_{n,k}(u) = H$ *and* $u(0) = u'(0) = 0$. *Then, there exists a constant* $K = K(a_0) > 0$ *independent of* F, H, u_γ, u *and* γ *such that*

$$\|u_\gamma - u\|_{H^2(0,1)} \leqslant K \left(\|F - H\|_{L_2(0,1)} + \sqrt{\gamma} \|u\|_{H^4(0,1)} \right).$$

The proof of lemma 5.2 is based on lemma 5.1, the Riesz theorem and the variational principle. The main difference between lemma 5.1 and Carleman estimates for elliptic operators in the $n{-}\mathrm{D}$ ($n \geqslant 2$) case is that we now have the integration on the right-hand side of (5.29) over the entire interval $(0, 1)$ rather than over a subdomain of the original domain in $n{-}\mathrm{D}$ [34]. The absence of local minima of the functional (5.28) follows from lemma 5.2. It can be derived from lemma 5.1 that it is not necessary to use the regularization term $\gamma \|q_{n,k}\|_{H^4(0,1)}^2$ in (5.28). Still, we use this term to ensure that functions $\varepsilon_r^{(n,k)} \in C^1[0, 1]$. Although lemma 5.1 implies that it is not necessary to use the condition $q'_{n,k}(1) = 0$, we still use it in our computations to improve the stability.

5.4. A brief scheme of the numerical method

For the convenience of the reader, we present in this subsection a brief summary of the above numerical method by outlining its main steps.

Step 1. Calculate the Laplace transform (2.7) $\mathcal{L}g = \varphi(s)$ of the data $g(t)$ in (2.6).

Step 2. Using the function $\varphi(s)$ as well as formulas (5.3) and (5.5), calculate the boundary data $\psi_0(s) := q(0, s)$, $\psi_1(s) := q_x(0, s)$, $s \in [\underline{s}, \overline{s}]$ in (5.9) for the function $q(x, s) = \partial_s \{s^{-2} \ln [(w/w_0)(x, s)]\}$. Set $q_0(x) \equiv 0$. Let $\{q_n(x)\}_{n=1}^N$ be functions generated by the function $q(x, s)$, as defined in (5.12). Use (5.17) to calculate the boundary data for these functions at $\{x = 0\}$, $\psi_{0,n} := q_n(0)$, $\psi_{1,n} := q'_n(0)$.

Step 3. Calculate the first tail function $V_0(x)$ as in subsection 6.2. Set $V_{1,1}(x) := V_0(x)$.

Step 4. Given $n \in [1, N]$, $k \in [1, m]$, calculate the function $q_{n,k}(x)$. To do this, find an approximate solution of equation (5.15) with boundary conditions (5.16), using the QRM, via the minimization of the functional (5.28), subject to boundary conditions (5.16). As soon as the function $q_{n,k}(x)$ is approximately calculated, find the approximation $\varepsilon_r^{(n,k)}(x)$ for the unknown coefficient $\varepsilon_r(x)$ via formulas (5.21)–(5.23). Next, find the function $\widehat{\varepsilon}_r^{(n,k)}(x)$ via (5.24). In formulas (5.21)–(5.24), the index '1' should be replaced with the index 'k'.

Step 5. Solve the forward problem (2.8) and (2.9), with $s := \overline{s}$ and $\varepsilon_r(x) := \widehat{\varepsilon}_r^{(n,k)}(x)$. Next, calculate the new tail function $V_{n,k+1}(x)$ using (5.26), where indices $(n, 1)$ and $(n, 2)$ should be replaced respectively with (n, k) and $(n, k + 1)$.

Step 6. If $k < m$, then go to step 4 with $k := k + 1$. If, however, $k = m$ and $n < N$, then use (5.27). Next, set $V_{n+1,1}(x) := V_n(x)$ and go to step 4 with $n := n + 1$, $k := 1$. Finally, if $k = m$ and $n = N$, then set the approximate solution of the above CIP as $\varepsilon_{r,\mathrm{glob}}(x) := \varepsilon_r^{(N,m)}(x)$ (see definition 4.1) and stop the iterative process.

6. Convergence analysis

6.1. The exact solution

Using again the concept of Tikhonov for ill-posed problems [6, 22, 25, 46], we assume that there exists a unique exact solution $\varepsilon_r^*(x)$ of our CIP with the 'ideal' noiseless data $g^*(t)$ in (2.6), and the function $\varepsilon_r^*(x)$ satisfies conditions (2.1) and (2.2). Then $\varepsilon_r^*(x)$ generates functions, which are defined similarly with the ones above, $q_0^* \equiv 0$,

$$r^*(x, s), V^*(x, \bar{s}) := r^*(x, \bar{s}), q^*(x, s) = \partial_s r^*(x, s), q_n^*(x), \psi_{0,n}^*, \psi_{1,n}^*, n \in [1, N]. \qquad (6.1)$$

Similarly with (5.15) and (5.16), we obtain from (5.8) and (5.9),

$$
\partial_x^2 q_n^* - \left(A_{1,n} h \sum_{j=0}^{n-1} \partial_x q_j^* - A_{1,n} \partial_x V^* - 2A_{2,n} \right) \partial_x q_n^* = -A_{2,n} h^2 \left(\sum_{j=0}^{n-1} \partial_x q_j^* \right)^2 + 2h \sum_{j=0}^{n-1} \partial_x q_j^*
$$

$$
+ 2A_{2,n} \partial_x V^* \left(h \sum_{j=0}^{n-1} \partial_x q_j^* \right) - A_{2,n} \left(\partial_x V^* \right)^2 + 2A_{2,n} \partial_x V^*
$$

$$
+ F_{1,n}(x, \mu, h, \bar{s}), \quad x \in (0, 1), \qquad (6.2)
$$

$$q_n^*(0) = \psi_{0,n}^*, \partial_x q_n^*(0) = \psi_{1,n}^*, \partial_x q_{n,k}^*(1) = 0. \qquad (6.3)$$

In (6.2), $F_n(x, \mu, h)$ is the error function which is generated by averaging (5.17) of the boundary functions ψ_0^* and ψ_1^*. Also, the nonlinear term $B_n(\mu, h)\left(\partial_x q_n^*\right)^2$ is included in $F_{1,n}$. By embedding theorem there exists a constant $C_2 \geqslant 1$ such that

$$\|f\|_{C[0,1]} \leqslant C_2 \|f\|_{H^1(0,1)}, \quad \forall f \in H^1(0, 1). \qquad (6.4)$$

By the above-mentioned concept of Tikhonov for ill-posed problems, we can assume that we know a number $C^* > 0$ such that

$$\max_{n \in [1,N]} \|q_n^*\|_{C^1[0,1]} \leqslant \frac{C^*}{C_2}, \quad \max_{n \in [1,N]} \|q_n^*\|_{H^4(0,1)} \leqslant C^*. \qquad (6.5)$$

6.2. Approximate mathematical model

Following definition 4.1, we introduce in this subsection an approximate mathematical model. Assumptions of this model are based on the asymptotic formulas (5.10) and (5.11). These assumptions actually mean that we consider only the first term of the asymptotic behavior of the tail function $V^*(x, \bar{s})$ when the pseudofrequency $\bar{s} \to \infty$ and truncate the rest. We call $\bar{s}$ the *truncation pseudofrequency*. A similar assumption is used in, e.g. geometrical optics. Our approximate mathematical model consists of the following two assumptions.

1. Let the parameter $\bar{s} > 1$. Then, there exists a function $a^* \in H^4(0, 1)$ such that the function $V^*(x, s)$ has the form

$$V^*(x, s) = s^{-1} a^*(x), \quad \forall s \geqslant \bar{s}, \quad \forall x \in [0, 1]. \qquad (6.6)$$

2. The following equality holds:

$$\bar{s}^{-1} a^*(x) = \bar{s}^{-2}[\ln w^*(x, \bar{s}) - \ln w_0(x, \bar{s})]. \qquad (6.7)$$

Compare (6.6) and (6.7) with (5.7) and (5.11). Using the third condition (6.1) and (6.7), we obtain

$$q^*(x, \bar{s}) = -\bar{s}^{-2} a^*(x). \qquad (6.8)$$

15

Consider equation (5.8) for the pair $(q^*(x, s), V^*(x, \bar{s}))$, $s \in [\underline{s}, \bar{s}]$. Then, the boundary conditions (5.9) are valid with functions $\psi_0^*(s)$ and $\psi_1^*(s)$. Hence, substituting in (5.8) and (5.9) $s := \bar{s}$ and using (6.8), we find that the function $a^*(x)$ is the solution of the following overdetermined boundary value problem:

$$\partial_x^2 a^*(x) = 0, \quad x \in (0, 1), \tag{6.9}$$

$$a^*(0) = -\bar{s}^2 \psi_0^*(\bar{s}), \quad \partial_x a^*(0) = -\bar{s}^2 \psi_1^*(\bar{s}), \quad \partial_x a^*(1) = 0. \tag{6.10}$$

In (6.10), exact boundary data at $x = 0$ are used. In practice, however, we have the non-exact data boundary $\psi_0(s)$, $\psi_1^*(s)$. Hence, consider the following boundary value problem for the function $a(x)$:

$$\partial_x^2 a(x) = 0, x \in (0, 1), \tag{6.11}$$

$$a(0) = -\bar{s}^2 \psi_0(\bar{s}), \quad \partial_x a(0) = -\bar{s}^2 \psi_1(\bar{s}), \quad \partial_x a(1) = 0. \tag{6.12}$$

We solve problem (6.11) and (6.12) via the QRM (see remark 5.1). Let the function $a_\gamma \in H^4(0, 1)$ be the unique minimizer of the following analogue of the QRM functional (5.28):

$$\bar{J}_\gamma(a) = \|a''\|_{L_2(0,1)}^2 + \gamma \|a\|_{H^4(0,1)}^2, \tag{6.13}$$

subject to boundary conditions (6.12). Because of (6.6)–(6.13), we define the first guess for the tail function as

$$V_0(x) = \bar{s}^{-1} a_\gamma(x). \tag{6.14}$$

Let $\sigma \in (0, 1)$ be the level of the error in the boundary data. We assume that

$$|\psi_0(\bar{s}) - \psi_0^*(\bar{s})| + |\psi_1(\bar{s}) - \psi_1^*(\bar{s})| \leqslant \sigma. \tag{6.15}$$

Remark 6.1. Let $a_\gamma(x)$ be the approximate solution of problem (6.11)–(6.13). Then, substituting (6.14) into (5.1) and (5.6) at $s = \bar{s}$, one can find a good approximation for the exact coefficient $\varepsilon_r^*(x)$. Furthermore, theorem 6.1 implies that all functions $\varepsilon_r^{(n,k)}$ are good approximations for $\varepsilon_r^*(x)$, as long as the total number of iterations is not too large. This corresponds well with (4.1). Since we find $a_\gamma(x)$ only using the boundary data, this means that our approximate mathematical model is indeed a good one. Hence, we can stop iterations on any function $\varepsilon_r^{(n,k)}$ for those indices (n, k), which are 'allowed' by theorem 6.1. Next, one can use the adaptivity procedure to refine the solution (the end of subsection 4.1). This was confirmed numerically in tests 2 and 3 of [7] as well as in tests 2 and 3 in section 4.16.2 of [6]. However, if not using the adaptivity for refinement, then, quite naturally, one needs to find an optimal iteration number to stop; see figures 7.3, 7.5, 7.6 and 7.8 of [5], figures 3 and 4 of [10], figures 6 of [26] and figure 1(b) of [30] (this again corresponds well with definition 4.1). These figures can also be found in chapters 3–5 of [6], along with objective stopping criteria for iterations.

Remark 6.2. Because of the approximate nature of equalities (6.6) and (6.7), equation (6.9) does not match the asymptotic behavior (5.10), which is the single self-contradiction of this approximate mathematical model. The same can be stated about all other versions of this method in the above cited publications. Nevertheless, it was consistently demonstrated that this numerical method works well for both computationally simulated and experimental data. Based on our numerical experience, we believe that this is because of two factors: (1) the truncation of the asymptotic series with respect to $1/\bar{s}$ at $\bar{s} \to \infty$ in (6.6) is reasonable and (2) the procedure of updating tail functions.

Lemma 6.1. *For each value of the regularization parameter, $\gamma \in (0, 1)$, there exists a unique minimizer $a_\gamma \in H^4(0, 1)$ of the functional (6.13) satisfying the boundary conditions (6.12). The following estimates hold:*

$$\|a_\gamma\|_{H^4(0,1)} \leqslant C\overline{s}^2\gamma^{-1/2}\left(|\psi_0(\overline{s})| + |\psi_1(\overline{s})|\right),$$

where the constant $C > 0$ is independent of $a_\gamma, \gamma, \overline{s}, \psi_0(\overline{s}), \psi_1(\overline{s})$. Let assumptions 1 and 2 hold and the function $a^* \in H^4(0, 1)$ be the solution of problems (6.9) and (6.10). Let (6.15) hold. Then, there exists a constant $K > 0$ independent of $a^*(x), a_\gamma(x), \gamma, \overline{s}, \psi_0(\overline{s}), \psi_1(\overline{s})$ such that

$$\|V_0 - V^*\|_{H^2(0,1)} \leqslant K\overline{s}(\sigma + \sqrt{\gamma}\|a^*\|_{H^4(0,1)}).$$

This lemma easily follows from lemma 5.2, (5.5) and (6.6)–(6.14). Uniqueness within the framework of this approximate mathematical model can be easily derived; see lemma 6.6.2 in [6] for a similar result. We assume below that the above exact solution $\varepsilon_r^*(x)$ is exactly the same as the one within the framework of this model, i.e.

$$\varepsilon_r^*(x) = r_{xx}^* + s^2\left(r_x^*\right)^2 - 2sr_x^* + 1, \quad s \in [\underline{s} \quad \overline{s}], \quad x \in [0, 1]; \tag{6.16}$$

see (5.1). Here, the function r^* is defined via (5.6) and (5.7), where the functions q and V are replaced with the functions $q^*(x, s)$ and $V^*(x, \overline{s})$, and (6.6)–(6.8) hold. Hence, (6.2)–(6.4) and (6.16) imply the following analogues of the discrete formulas (5.21) and (5.22):

$$r_n^*(x) = -hq_n^*(x) - h\sum_{j=0}^{n-1} q_j^*(x) + V^*(x, \overline{s}) + F_{2,n}(x, h, \overline{s}), \quad x \in [0, 1], \tag{6.17}$$

$$\varepsilon_r^*(x) = 1 + \partial_x^2 r_n^*(x) + s_n^2\left[\partial_x r_n^*(x)\right]^2 - 2s_n\partial_x r_n^*(x) + F_{3,n}(x, h, \overline{s}), \quad x \in [0, 1]. \tag{6.18}$$

One can prove that

$$\sum_{j=1}^{3} \|F_{j,n}\|_{L_2(0,1)} \leqslant C_1\overline{s}^2(h + \mu^{-1}), \tag{6.19}$$

where the constant $C_1 > 0$ is independent of $h, \mu, \overline{s}$. We assume that

$$F_{j,n} \equiv 0, j = 1, 2, 3; \psi_{0,n} = \psi_{0,n}^*, \psi_{1,n} = \psi_{1,n}^*, n \in [1, N]. \tag{6.20}$$

Therefore by (6.15) the error is 'allowed' only in numbers $\psi_0^*(\overline{s})$ and $\psi_1^*(\overline{s})$. We point out that an analogue of theorem 6.1 can be proved very similarly for the realistic case (6.19) and when $\left|\psi_{0,n} - \psi_{0,n}^*\right|, \left|\psi_{1,n} - \psi_{1,n}^*\right| < \sigma$. So, condition (6.20) is introduced for brevity only. An additional simplification of the presentation comes from balancing the error parameters h and σ with the regularization parameter γ and parameters ξ and μ in (5.13) and (5.19) as

$$\sigma = \sqrt{\gamma} = \sqrt{2\xi} = \mu^{-1} := h. \tag{6.21}$$

6.3. Approximate global convergence theorem

The main new element of theorem 6.1 is that we iteratively estimate tails, which was not done in [30]. To do this, we use (3.25) and (3.26). The proof of theorem 6.1 has some similarities with the proof of theorem 6.7 of [6] for the 3D case. However, estimates of the H^2 -norm of the QRM solution $q_{n,k}$ in [6] are obtained in a subdomain of the domain Ω . In turn, this leads to the estimate of the accuracy of the computed target coefficient in another subdomain of Ω rather than in the entire Ω . On the other hand, because of the 1D case, (5.29) implies a stronger estimate of that accuracy in the whole interval $(0, 1)$. Still, because of the above similarity with the proof of theorem 6.7 of [6], and also because the proof of theorem 6.1 is rather technical, we only outline it here.

17

Theorem 6.1 (Approximate global convergence). *Let the function $\varepsilon_r^*(x)$ satisfying conditions (2.1) and (2.2) be the exact solution of our CIP for the noiseless data $g^*(t)$ in (2.6). Fix the truncation pseudo frequency $\bar{s} > \max(\hat{s}(d, |x_0|), 1)$, where the number $\hat{s}(d, |x_0|)$ was defined in theorem 3.1. Let two assumptions of subsection 6.2 hold and $\|a^*\|_{H^4(0,1)} \leqslant C^*$, where C^* is the constant defined in (6.5). Let the first tail function $V_0(x)$ be defined via (6.11)–(6.14). In addition, let conditions (6.15), (6.20) and (6.21) hold. Let $B = B(x_0, d, \bar{s}) > 1, C_2, C^*$ and K be the numbers defined in theorem 3.2, (6.4), (6.5) and lemma 6.1. Define $B_1 = B_1(x_0, d, \bar{s}) = \max(C_2, B, C^*, K\bar{s})$. Consider the iterative process of subsection 5.2. Let the number $N \geqslant 2$ be independent of h. Then there exists a constant $D = D(x_0, d, \bar{s}) \geqslant 32\bar{s}^2 B_1$ such that if for a constant $b > 1$ independent of $x_0, d, \bar{s}$,*

$$h \in (0, h_0), \quad h_0 = \frac{1}{bD^{2Nm+2}}, \tag{6.22}$$

then the following estimates are valid:

$$\left\| q_{n,k} - q_n^* \right\|_{H^2(0,1)} \leqslant D^{(n-1)m+k+2} h, \tag{6.23}$$

$$\left\| q_{n,k} \right\|_{C^1[0,1]} \leqslant 2C^*, \tag{6.24}$$

$$\left\| \varepsilon_r^{(n,k)} - \varepsilon_r^* \right\|_{L_2(0,1)} \leqslant D^{(n-1)m+k+1} h, \tag{6.25}$$

$$\|V_{n,k}' - \partial_x V^*\|_{L_2(0,1)} + \|V_{n,k}'' - \partial_x^2 V^*\|_{L_2(0,1)} \leqslant D^{(n-1)m+k+1} h, \tag{6.26}$$

$$\left\| V_{n,k}' \right\|_{C[0,1]} \leqslant 2B_1, \tag{6.27}$$

$$\left| A_{1,n} h \sum_{j=0}^{n-1} q_j' - A_{1,n} V_{n,k}' - 2A_{2,n} \right|_{C[0,1]} \leqslant 18\bar{s}^2 B_1 := a_0. \tag{6.28}$$

Here, $q_{n,k}$ are the QRM solutions of the boundary value problems (5.15) and (5.16). In particular, let the number $\omega \in (0, 1)$ be defined as

$$\omega = \frac{\ln b}{\ln b + (2Nm + 2)\ln D}.$$

Then (6.25) implies the Hölder-like estimate

$$\left\| \varepsilon_r^{(n,k)} - \varepsilon_r^* \right\|_{L_2(0,1)} \leqslant h^\omega := \theta,$$

which guarantees the approximate global convergence property of the level θ of this iterative process within the framework of the approximate mathematical model of subsection 6.2 (definition 4.1).

Remark 6.3. Since the number N of s subintervals (s_i, s_{i-1}) is assumed to be independent of the partition step size h, then theorem 6.1 requires the length of the total s interval $[\underline{s}, \bar{s}]$ covered in the iterative process of subsection 5.2 to decrease with the decrease of h. This seems to be a natural requirement. Indeed, if the number $\bar{s} - \underline{s}$ would be independent of h, then this would mean the increase of the number of iteration $Nm = m \cdot (\bar{s} - \underline{s})/h$. On the other hand, the error increases with the iteration number, especially for nonlinear ill-posed problems. Hence, the number of iterations Nm is one of the regularization parameters here. It was pointed out on pages 156–7 of [22] that the total number of iterations can often be regarded as a regularization parameter in the theory of ill-posed problems. Two other regularization parameters are $\bar{s}$ and γ. Thus, we have a vector $(Nm, \bar{s}, \gamma)$ of regularization parameters.

Remark 6.4. Another argument justifying the smallness of the interval $[\underline{s}, \overline{s}]$ is that the original equation (5.8) contains Volterra-like integrals in nonlinear terms. It is well known from the standard ODE course that the existence of the solutions of Volterra-like integral equations is guaranteed only on sufficiently small intervals.

Outline of the proof of theorem 6.1. To avoid using new notation, below $q_{n,k}(x)$ means the QRM solution of problem (5.15) and (5.16). The only exception is when we subtract (6.2) and (6.3) from (5.15) and (5.16), respectively. Denote

$$\widetilde{q}_{n,k} = q_{n,k} - q_n^*, \widetilde{\varepsilon}_r^{(n,k)} = \varepsilon_r^{(n,k)} - \varepsilon_r^*, \widetilde{V}_{n,k} = V_{n,k} - V^*.$$

Consider the case $(n, k) = (1, 1)$. First, by lemma 6.1

$$\left\| \widetilde{V}_{1,1}' \right\|_{L_2(0,1)} + \left\| \widetilde{V}_{1,1}'' \right\|_{L_2(0,1)} \leqslant B_1 h < D^2 h. \tag{6.29}$$

Hence, (3.25), (6.4), (6.22) and (6.29) imply that

$$\left\| V_{1,1}' \right\|_{C[0,1]} = \left\| \widetilde{V}_{1,1}' + \partial_x V^* \right\|_{C[0,1]} \leqslant C_2 D^2 h + B_1 \leqslant 2B_1. \tag{6.30}$$

Estimates (6.29) and (6.30) establish (6.26) and (6.27) for $(n, k) = (1, 1)$. Consider now the function $\widetilde{q}_{1,1}$. Subtracting (6.2) from (5.15) and (6.3) from (5.16), using (6.20) and setting $n = k = 1$, we obtain

$$\widetilde{q}_{1,1}'' + \left(A_{1,1} V_{1,1}' + 2A_{2,1} \right) \widetilde{q}_{1,1} = -\left[A_{1,1} \partial_x q_1^* + A_{2,1} \left(V_{1,1}' + \partial_x V^* \right) \right] \widetilde{V}_{1,1}, x \in (0, 1), \tag{6.31}$$

$$\widetilde{q}_{1,1}(0) = \widetilde{q}_{1,1}'(0) = \widetilde{q}_{1,1}(1) = 0. \tag{6.32}$$

We now need to estimate the QRM solution $\overline{q}_{1,1}$ of problem (6.31) and (6.32). By (5.18), (6.29) and (6.30)

$$\left| A_{1,1} V_{1,1}' + 2A_{2,1} \right| \leqslant 8\overline{s}^2 (B_1 + 2) \leqslant \tfrac{1}{2} a. \tag{6.33}$$

Next, using (3.25), (5.18), (6.5), (6.29) and (6.30), we obtain

$$|A_{1,1} \partial_x q_1^* + A_{2,1}(V_{1,1}' + \partial_x V^*)| \leqslant 8\overline{s}^2(C^* + 3B_1) \leqslant 32\overline{s}^2 B_1,$$

$$\|[A_{1,1} \partial_x q_1^* + A_{2,1}(V_{1,1}' + \partial_x V^*)]\widetilde{V}_{1,1}'\| \leqslant 32\overline{s}^2 B_1^2 h \leqslant D^2 h. \tag{6.34}$$

We can take $D \geqslant K(a_0)$, where numbers a_0 and $K(a_0)$ are defined in (6.33) and lemma 5.2, respectively. Hence, lemma 5.2, (6.31), (6.32) and (6.34) imply that

$$\|\widetilde{q}_{1,1}\|_{H^2(0,1)} \leqslant D^3 h, \tag{6.35}$$

which proves (6.23) for $\widetilde{q}_{1,1}$. Next, to prove (6.24), we use (6.5), (6.22) and (6.35),

$$\|q_{1,1}\|_{C^1[0,1]} \leqslant C_2 \|q_{1,1}\|_{H^2(0,1)} \leqslant C_2 \|\widetilde{q}_{1,1}\|_{H^2(0,1)} + C_2 \|q_1^*\|_{H^2(0,1)} \leqslant 2C^*. \tag{6.36}$$

Next, subtract (6.18) from (5.22). Note that by (2.1) and (5.23)

$$\left| \widetilde{\varepsilon}_r^{(n,k)}(x) \right| = \left| \varepsilon_r^{(n,k)}(x) - \varepsilon_r^*(x) \right| \leqslant \left| \overline{\varepsilon}_r^{(n,k)}(x) - \varepsilon_r^*(x) \right|, \quad \forall x \in [0, 1].$$

Hence, using (6.22), (6.29), (6.30), (6.35) and (6.36), we obtain

$$\|\widetilde{\varepsilon}_r^{(1,1)}(x)\|_{L_2(0,1)} \leqslant (D^3 h^2 + B_1 h)(1 + \overline{s}^2(3C^*h + 3B_1 + 2))$$
$$\leqslant 7\overline{s}^2(D^3 h^2 + B_1 h) \leqslant 14\overline{s}^2 Dh \leqslant D^2 h,$$

which establishes (6.25) for $n = k = 1$. Next, using (3.26), (5.19), (5.24) and (6.21), we obtain

$$\left\| \widetilde{V}_{1,2}' \right\|_{L_2(0,1)} + \left\| \widetilde{V}_{1,2}'' \right\|_{L_2(0,1)} \leqslant 2BD^2 h + \sqrt{2\xi} d \leqslant D^3 h.$$

Hence, similarly with (6.30) $\left\| V_{1,2}' \right\| \leqslant 2B_1$. Thus, (6.26) and (6.27) are established for $n = 1, k = 2$. The rest of the proof can be done similarly using mathematical induction. We need (6.28) to estimate norms $\left\| \widetilde{q}_{n,k} \right\|_{H^2(0,1)}$ via lemma 5.2. The estimate (6.28) is proved using (5.18), (6.22) and (6.24). $\qquad\square$
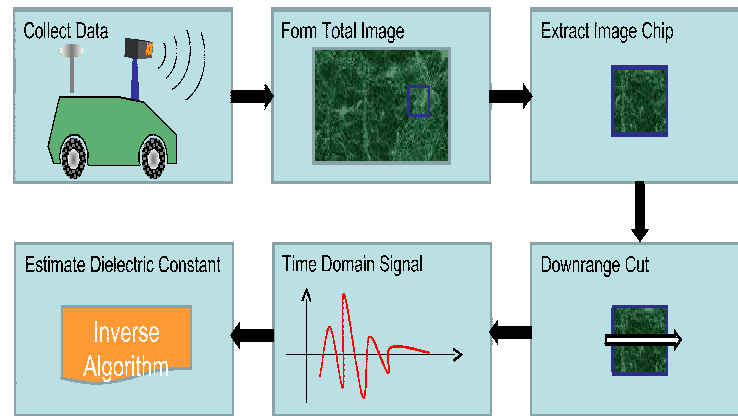
Figure 1. A schematic diagram of data collection by the Forward Looking Radar of the US Army Research Laboratory.

7. Experimental setup and data pre-processing

7.1. Data collection

A schematic diagram of the data collection by the Forward Looking Radar is depicted in figure 1. Time-resolved electric pulses are emitted by two sources installed on the radar. Only one component of the electric field is both originated and measured in the backscattering regime. The data are collected by 16 detectors with a step size in time of 0.133 ns. Only shallow targets placed both below and above the ground can be detected. The depth of the upper part of a shallow underground target is a few centimeters. A ground positioning system (GPS) provides the distance between the radar and a point on the ground located above that target. The error in the latter is of a few centimeters. Time-resolved voltages of backreflected signals are integrated over radar/target distances between 20 and 8 m, and they are also averaged with respect to both source positions and with respect to readings of 16 detectors. Since the radar/target distance is known, it is approximately known which part of the measured time-resolved signal corresponds to the reflections from that target; see figure 1. However, clutter obviously obscures a significant part of that signal. For any target of interest, only a single time-dependent curve can be extracted from the vast amount of data; see samples in figures 4(b), (d) and (f). This is the curve we have worked with in each of the available five cases of experimental data.

Since the radar/target distance is provided by the GPS with a good accuracy, geometrical parameters of targets, including their depths, are not of interest here. The *main goal* of our work was to calculate ratios R of dielectric constants

$$R = \frac{\varepsilon_r(\text{target})}{\varepsilon_r(\text{bckgr})},\tag{7.1}$$

where ε_r (bckgr) is the dielectric constant of the background medium. If ε_r (bckgr) is known, then (7.1) enables us to calculate ε_r (target). If a target is located above the ground, then ε_r (bckgr) = ε_r (air) = 1. Since targets can be mixtures of constituent materials, the ε_r (target) is a certain weighted average of dielectric constants of these materials. We image the ratio (7.1) rather than the function $\varepsilon_r(x)$ itself, since (2.1) requires that ε_r (bckgr) should have a constant value outside of our domain of interest $x \in (0, 1)$. The latter was true only for targets located

above the ground. However, in the case of underground targets, this condition is invalid because of the air/ground interface. Below '1' stands for '1 m'.

A separate question is about the meaning of the dielectric constant in metallic targets. Comparison of figures 2(a) and (b) shows that the electric field reflected from the metallic target is about the same as that reflected from the dielectric target with a large value of the dielectric constant. Next, we simulated the data for four large inclusion/background contrasts by solving (2.8) and (2.9). Figure 2(c) shows the computed functions $w(0, s) - w_0(0, s), s \in [1, 12]$ for the case of a single inclusion embedded in the interval $(0, 1)$ with four different values of the function $\varepsilon_r = 10, 20, 30, 40$ in this inclusion; see figure 3(a) for the geometry. One can observe that these curves do not change much with a change of $\varepsilon_r \in [10, 30]$. Furthermore, curves for $\varepsilon_r = 30, 40$ are almost the same. Therefore, based on figures 2(a)–(c), we choose interpretation (7.2) of the dielectric constant in metals. The physical meaning of (7.2) is unknown, and we call it *appearing dielectric constant for metals*,

$$\varepsilon_r(\text{metal}) \in [10, 30]. \tag{7.2}$$

7.2. Main uncertainties in the experimental data

To figure out what kind of ideal data one should expect for the case of one target only, we performed computational simulations via solving the forward problem (2.3) and (2.4) for the case of one target and for the source position

$$x_0 = -1. \tag{7.3}$$

In data simulation, we replaced $\mathbb{R}$ in (2.3) with the interval $x \in (-6, 6)$ and have considered zero Dirichlet boundary conditions for rather small times,

$$u(-6, t) = u(6, t) = 0, t \in (0, 4). \tag{7.4}$$

Condition (7.4) is imposed because the wave front originated at the source position (7.3) does not reach points $x = \pm 6$ for $t \in (0, 4)$. The structure of the medium and the computed function $u(0, t) := g(t)$ are depicted in figures 3(a) and (b), respectively. In the case $\varepsilon_r(\text{target}) = \text{const.} \in (0, 1)$ the function $g(t)$ looks similar (not shown), except that its peak points downwards. Note that the constant background in figures 3(a) and (b) corresponds to the fundamental solution of the 1D wave equation $v_{tt} = v_{xx}$,

$$u_0(x, t) = \tfrac{1}{2}H(t - |x - x_0|),$$

where H is the Heaviside function. Figures 4(b), (d) and (f) show the experimental data for different targets. A visual comparison of figures 4(b), (d) and (f) with figure 3(b), confirms the above mentioned (section 1) *substantial discrepancy* between computationally simulated and experimental data. This discrepancy is the main challenge of working with these data.

In addition to the above misfit and the 3D reality versus only a single curve for each target, there were some other uncertainties here as well. The most significant uncertainties were as follows.

(1) The reference signal was not measured.
(2) The direction of the incident plane wave was oblique to the ground rather than orthogonal; see figures 4(a), (c) and (e).
(3) Units for the amplitude of experimental data were unknown.
(4) The location of the point source x_0 was unknown. Thus, (7.3) is an intuitive choice.
(5) The time moment $t = 0$ on the data was unknown.
(6) The background was heterogeneous due to clutter.
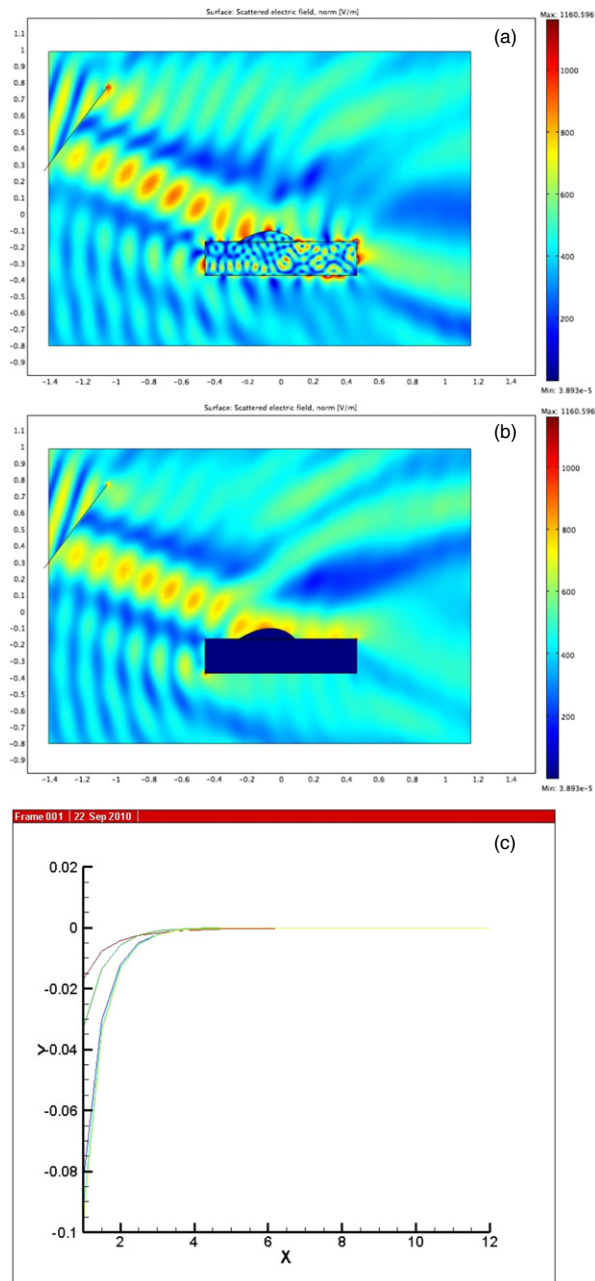
Figure 2. Appearing dielectric constant for metals for computationally simulated data at a single frequency. (a) The amplitude of the electric field reflected from a dielectric target with $\varepsilon_r = 10$ in it. (b) The amplitude of the electric field reflected from a metallic target of the same frequency as that of (a). Reflected fields (a) and (b) are very similar. (c) Computed functions $(w - w_0)(0, s)$, $s \in [1, 12]$ for the case when one inclusion is embedded in the interval $(0, 1)$ with different values of the function ε_r; see figure 3(a) for the location of the inclusion. From top to bottom $\varepsilon_r = 10, 20, 30, 40$. Curves for $\varepsilon_r = 30, 40$ almost coincide. Hence, the function $w(0, s)$ does not change much with an increase in the inclusion/background contrast from 10 to 40. (a)–(c) justify definition (7.2) of the appearing dielectric constant for metals.

(a)   (b)
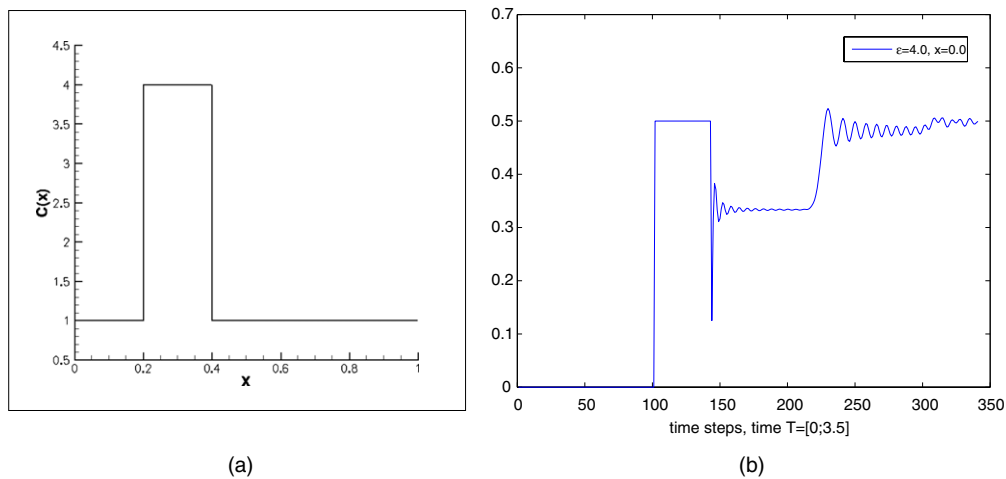
Figure 3. Computationally simulated data $u(0, t)$, where $u(x, t)$ is the solution of problem (2.1) and (2.2) with the source location $x_0 = -1$. Boundary conditions (7.4) were used, since the wave front did not yet reach points $x = \pm 6$ for times $t \in (0, 4)$. (a) The function $\varepsilon_r(x)$, $x \in (0, 1)$. Also, $\varepsilon_r(x) = 1$ for $x \notin (0, 1)$. (b) The function $u(0, t)$ in time $T = [0, 3.5]$.

Remark 7.1. It is because of items 4 and 5 that it was impossible to image locations of targets correctly.

At the same time, the UNCC/ChalmersGU team had the following two pieces of the information in advance.

(1) The presence of a single target for each data set.
(2) It was known whether the target was located above or below the ground.

7.3. Data pre-processing

We need to pre-process the experimental data in such a way that the resulting time-resolved curves would look similar to figure 3(b), since this would fit, at least somehow, our mathematical model. If the target is located above the ground, then ε_r (target) > 1, since ε_r(bckgr) $= \varepsilon_r$ (air) $= 1$ in this case. Figure 3(b) indicates that one should select on the experimental curve only one downward-looking peak in this case. However, if the target is buried in the ground, then there could be any relation between ε_r(target) and ε_r(bckgr). Hence, based on figures 3(a) and (b) as well as their analogues for the case ε_r(target) $< \varepsilon_r$(bckgr) (not shown), we selected on each experimental curve the earliest peak of the largest amplitude out of all other peaks. The rest peak of each curve was set to zero. More precisely, our selection of that peak was as follows: this should be the earliest peak of the largest amplitude

$$\text{out of } \begin{cases} \text{all peaks for a target buried in the ground,} \\ \text{all downward-looking peaks for a target above the ground.} \end{cases}$$

We assigned on each experimental curve the time zero $\{t = 0\}$ to be such a point on the time axis, which is 1 ns off to the left from the beginning of the selected peak. Next, we multiplied the resulting data by the scaling factor (below) and have regarded the resulting curve as the pre-processed data. Figure 5(a) displays the pre-processed data for the case of figure 4(b).

23
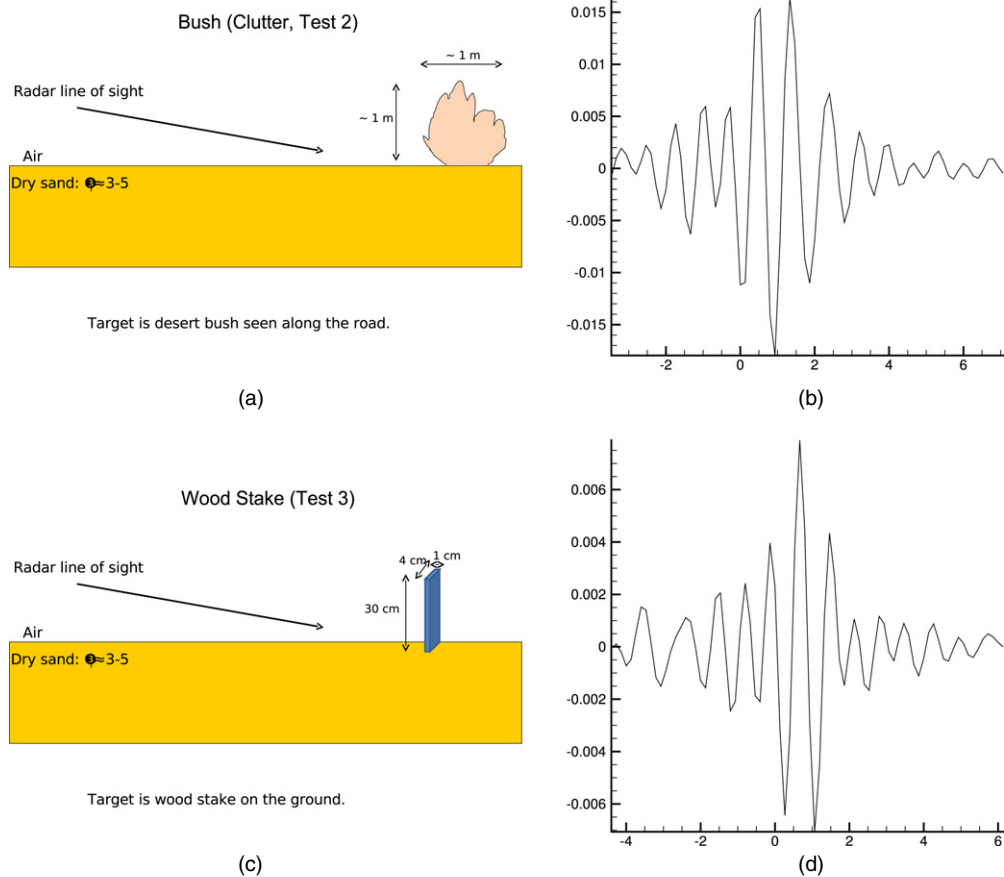
Figure 4. Targets and experimental data for tests 1–3. The ground is dry sand with $\varepsilon_r \in [3, 5]$ [44]. Because of the blind study case, (a), (c) and (e) were released to the UNCC/ChalmersGU team only after computations were made. (a) Bush standing along the road (clutter). (b) Scaled experimental data for (a) (subsection 7.3). The horizontal axis is time in nanoseconds with a time step of 0.133 ns. The vertical axis is the amplitude of the measured voltage. (c) Wood stake. (d) Scaled experimental data for (c). (e) Metal box buried in the dry sand. (f) Scaled experimental data for (e). The amplitude of the largest downward-looking peak on (f) is 0.0072, whereas the amplitude of the largest upward-looking peak is 0.007. Therefore, the downward-looking peak was used in our data pre-processing. A huge misfit between experimental and computationally simulated data is evident: compare highly oscillatory curves of (b), (d) and (f) with figure 3(b). Waveforms of (b), (d) and (f) show why the radar detection and discrimination problem is so challenging. One can see three very different types of targets, yet their signatures are very similar.

Figure 5(b) shows superimposed pre-processed curves for all five cases of experimental data we possess.

   The amplitude of the time-resolved signal for each case was of the order of 10^5. This is well above the amplitude of figure 3(b). Thus, all pre-processed data were multiplied by the scaling number $SN = 10^{-7}$. Here we show how we have chosen the number $SN = 10^{-7}$. Consider the pre-processed signal for the bush and multiply it by 10^{-7}. We obtain the signal depicted in figure 5(a). Next, calculate the Laplace transform for $s \in [1, 5]$ of two signals: (1) that of figure 5(a) and (2) that of the computationally simulated data of figure 3(b). Superimposed graphs of the function $\widehat{w}(x, s) = w(0, s) - w_0(0, s), s \in [1, 5]$ for both these cases are
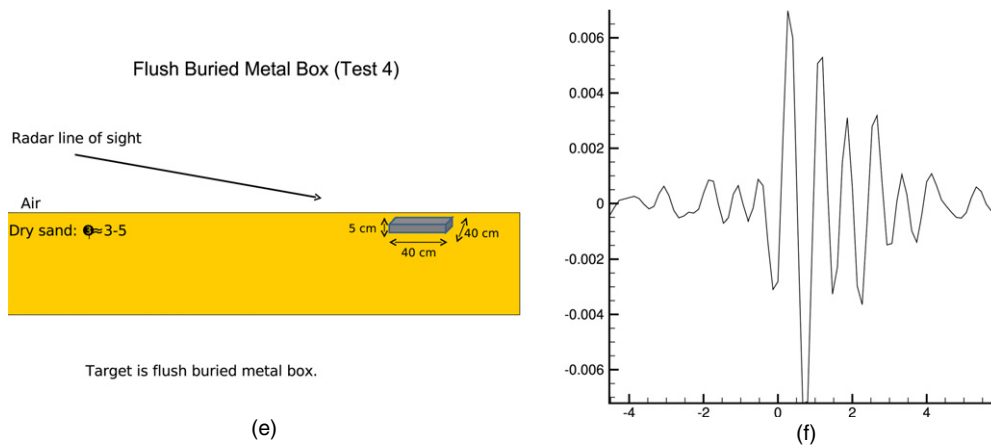
(e)

(f)

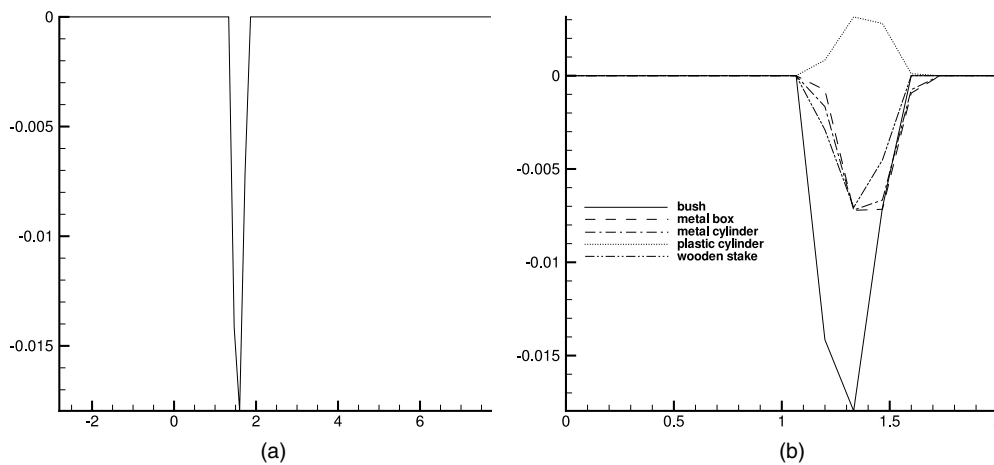**Figure 4.** (Continued.)

(a)

(b)

Figure 5. The horizontal axis is time in nanoseconds with a time step size of 0.133 ns. (a) The pre-processed experimental data for the bush standing along the road (clutter); see figures 4(a) and (b). (b) The pre-processed experimental data for all five cases (superimposed). In terms of our mathematical model, we use these curves as functions $u(0, t) - u_0(0, t)$.

displayed in figure 6. One can observe in this figure that minimal and maximal values of both curves are approximately the same.

In fact, we initially tried three scaling numbers: $SN_1 = 10^{-6}$, $SN_2 = 10^{-7}$ and $SN_3 = 10^{-8}$. In the end we have chosen $SN_2 := SN = 10^{-7}$ out of these three. We have made this choice because of our observation that this was the only case out of three when minimal and maximal values of functions $\widehat{w}(x, s)$, $s \in [1, 5]$ of both above curves: that of the Laplace transform of the function depicted in figure 3(b) and that of the Laplace transform of the function of figure 5(a), were approximately the same, see figure 6. On the other hand, for SN_1 and SN_3 the minimal and maximal values were quite different from those of the Laplace transform of the function of figure 3(b). As soon as $SN = 10^{-7}$ was chosen, using only the data for the bush, we multiplied the other four pre-processed signals by 10^{-7}, and observed similar behavior of the minimal and maximal values of the Laplace transforms of the resulting four functions. So, the graphs of figure 5(b) represent five available pre-processed signals being multiplied by 10^{-7}.
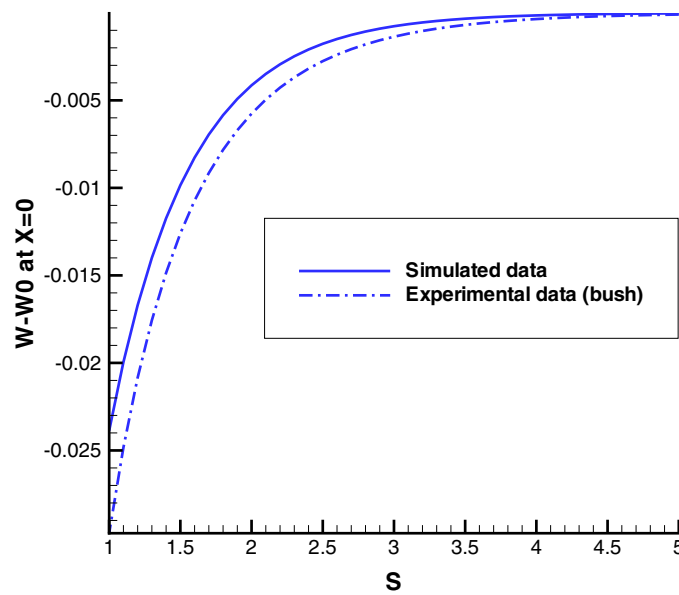
Figure 6. Graphs of the function $\widehat{w}(x, s) = w(0, s) - w_0(0, s)$, $s \in [1, 5]$ for the Laplace transform of the computationally simulated data for the function $\varepsilon_r(x)$ displayed in figure 3(a) and for the signal of the bush of figure 5(a). Recall that graphs of figures 5(a) and (b) were obtained after multiplying the pre-processed signals by the scaling number $SN = 10^{-7}$. One can observe that minimal and maximal values of the function $\widehat{w}(x, s)$ are approximately the same for both cases. A similar observation was in place for four other cases of figure 5(b).

In the case of the upward-looking peak of figure 5(b), we compared the function $|\widehat{w}(x, s)|$ for it with the function $\widehat{w}(x, s)$ for the simulated data above. Graphs of figures 4(b), (d) and (f) were obtained from original experimental curves by multiplying them by $SN = 10^{-7}$. In addition, we conducted a limited sensitivity study with respect to the scaling factor; see test 2 in sections 8 and 9.

7.4. Functions $\psi_0(s)$ and $\psi_1(s)$

Let $\widetilde{g}(t)$ be the pre-processed experimental data for any of our targets. Based on figure 5, we calculated the Laplace transform (2.7) $\varphi(s) = \mathcal{L}(g)$ by integration over the interval $t \in (0, 2)$. Next, we calculated the derivative $\varphi'(s)$ as

$$\varphi'(s) = -\int_0^2 \widetilde{g}(t) \, t \, e^{-st} \, dt + \partial_s w_0(0, s), \tag{7.5}$$

where the function $w_0(0, s)$ is defined in (2.11). It was observed in computational simulations of [30] that the function $\varphi(s)$ has the best sensitivity to the presence of inclusions for $s \in [0.5, 1.2]$. Nevertheless, we observed that the larger interval $s \in [1, 12]$ provides better quality images for simulated data. The function $\varphi(s)$ was computed accurately for the entire interval $s \in [1, 12]$ with the step size $\Delta s = 0.05$ in the s-direction. However, because of their dependence on the derivative $\varphi'(s)$ in (7.5), functions $\psi_0(s) = q(0, s)$, $\psi_1(s) = q_x(0, s)$ have oscillated for $s \in [3, 12]$. On the other hand, our testing of computationally simulated data has shown that oscillations should not be present.

Hence, we pre-processed the function $\psi_0(s)$ as follows. First, we calculated $\psi_0(s)$ for $s \in [1, 2.5]$ using the Laplace transform of the data, as in (7.5), with the 0.5 step size with respect to s. Next, we set $\psi_0(12) := 0.025 \cdot \psi_0(2.5)$, then we linearly interpolated the plane (s, ψ_0) between points $(2.5, \psi_0(2.5))$ and $(12, \psi_0(12))$ and similarly for $\psi_1(s)$. Having functions $\psi_0(s)$ and $\psi_1(s)$ for our pre-processed experimental data, we calculated numbers $\psi_{0,n}$ and $\psi_{1,n}$ in (5.17), which are used as boundary conditions for the QRM.

8. Imaging results

A detailed description of the numerical implementation of the algorithm of subsections 5.2 and 5.3 can be found in [30]. We now briefly outline the main elements as well as some differences with [30]. Unlike [30], where only synthetic data were used, the values $q_n(1)$ were unknown to us now (naturally). But this turned out not to be a problem. Indeed, our numerical experiments with computationally simulated data have shown to us that knowledge of the numbers $q_n(1)$ affects only the accuracy of the image of the location of a target. However, it does not affect the accuracy of the reconstruction of the target/background contrast in ε_r, which is our main goal here; see remark 7.1. Thus, unlike [30], we did not assign any values to $q_n(1)$. The initial tail function was taken as in (6.14). Although theorem 6.1 guarantees approximate global convergence only for the case of a small s interval, our computational experience tells us that the interval $s \in [1, 12]$ is an optimal one. We attribute this to the well-known fact that convergence estimates are routinely much more pessimistic than computational results. This is because constants in convergence theorems usually are largely overestimated. Similarly, although the above theory works only for the case $\varepsilon_r(x) \geqslant 1$, this did not prevent us from computing one case with $R < 1$ in (7.1).

We regard $R := R(x)$ in (7.1) as an x-dependent function. With respect to the results of this section, $\varepsilon_r(x)$ in (2.8) was replaced with $R(x)$. Thus, it is $R(x)$ which was computed by the above algorithm. Let $R_{\text{comp}}(x)$ be the computed coefficient $R(x)$. Then we define the computed target/background contrast as $\overline{R} = \max R_{\text{comp}}(x)$ in the case when $\max R_{\text{comp}}(x) > 1$, and as $\overline{R} = \min R_{\text{comp}}(x)$ in the case when $\max R_{\text{comp}}(x) \leqslant 1$. We set $\varepsilon_r(\text{target}) := \overline{R} \cdot \varepsilon_r(\text{bckgr})$.

For each test, we also computed two curves: the Laplace transform of the pre-processed experimental data and the function $w(0, s)$, where $w(0, s)$ is the solution of problem (2.8) and (2.9) with $\varepsilon_r(x) := R_{\text{comp}}(x)$. The interval $s \in [1, 12]$ with the step size $h = 0.5$ was used for the latter. These two curves were very close to each other for all tests.

Test 1. *Computationally simulated data*. First, we verify that our algorithm provides an accurate target/background contrast for computationally simulated data. We image the structure depicted in figure 3(a). Figure 7(a) displays the resulting image. Recall that we are interested in accurate imaging of target/background contrasts rather than in accurate imaging of locations of targets (subsection 7.1). The imaged target/background contrast is 3.8, whereas the real contrast is 4. Thus, the imaged contrast is quite accurate. This gives us a hope that contrasts for experimental data are also computed accurately.

Test 2. *The image of a bush* (see figures 4(a) and (b), 5(a) and (b)). This was the most difficult case because the target was a highly heterogeneous one. Moreover, the maximum of the modulus of the amplitude of the pre-processed signal for this target exceeds these values for other targets by a factor of 2.57. Figures 7(b) and (c) display the resulting image and the above superimposed curves, respectively. Only a small difference between the curves of figure 7(c) is observed.

We conducted a limited sensitivity study with respect to the choice of the scaling number *SN*. We varied *SN* by 20%. Figure 7(d) displays the computed function $R(x)$ for the data for the
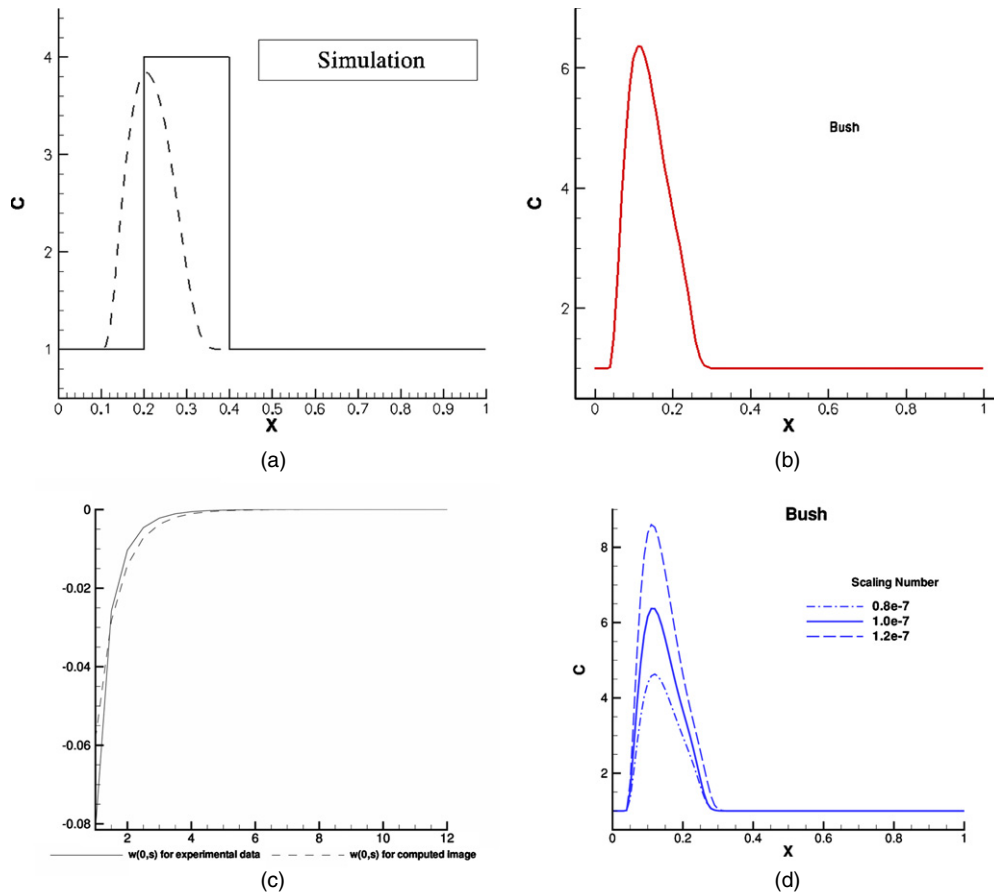
Figure 7. Resulting images. (a) The computed image for computationally simulated data (test 1). Solid and dashed lines are true and computed images, respectively. Recall that we are interested in accurate imaging of target/background contrasts rather than in accurate imaging of locations of targets (subsection 7.1). The computed target/background contrast is 3.8, which is 5% error. (b) The computed image of the bush; see figure 4(a). Here $\overline{R} = 6.4$, which is in the range of tabulated values $\varepsilon_r \in [3, 20]$ [20]. (c) The solid line is the Laplace transform of the function depicted in figure 5(a). The dashed line is the function $w(0, s) - w_0(0, s)$, where $w(0, s)$ is the solution of problem (2.8) and (2.9) with $\varepsilon_r(x) := R_{\mathrm{comp}}(x)$ of (b). (d) Results of a limited sensitivity study with respect to the choice of the scaling number $SN = 0.8 \times 10^{-7}, 10^{-7}, 1.2 \times 10^{-7}$ for the case of the bush (recall that we chose $SN = 10^{-7}$ for all our tests). One can observe that the computed value of $\overline{R}$ varies as $\overline{R} = 4.5, 6.4, 8.6$. All these three values are within tabulated limits; see table 1. A similar observation took place for four other targets we worked with. (e) The computed image of the wood stake (see figure 4(c)). Here $\overline{R} = 3.8$, which is in the range of tabulated values $\varepsilon_r \in [2, 6]$ (see [44]). (f) The computed image of the metal box, $\overline{R} = 3.8$.

bush obtained for $SN = 0.8 \times 10^{-7}, 10^{-7}, 1.2 \times 10^{-7}$. Recall that we chose $SN = 10^{-7}$ for all five sets of experimental data we possess (subsection 7.3). One can observe that corresponding values of the computed target/background contrast $\overline{R}$ are $\overline{R} = 4.5, 6.4, 8.6$. The value $\overline{R} = 6.4$ is for $SN = 10^{-7}$ and is, therefore, the same as that of figure 7(b). All these three values are within tabulated limits, see table 1. The same study was conducted for four other data sets we worked with. And the same observation was in place: the above three values of SN resulted
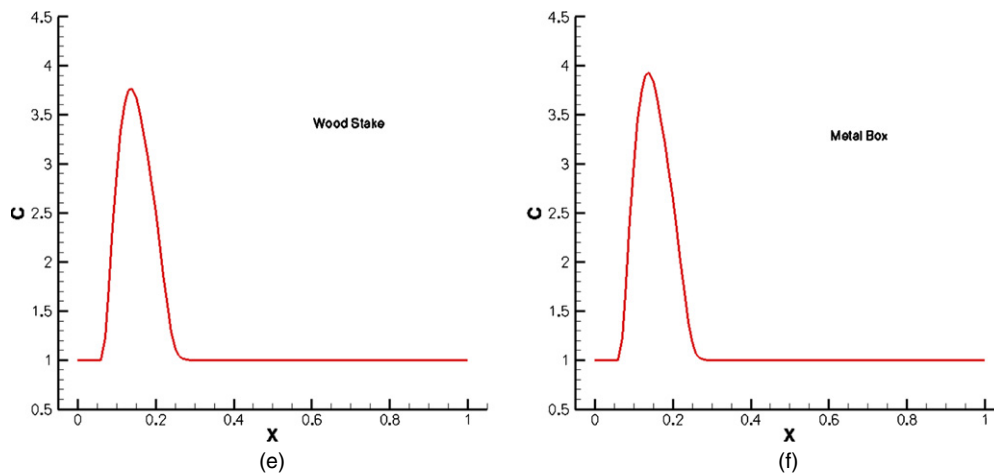
Figure 7. (Continued.)

Table 1. Blindly computed values $\overline{R}$ for five targets, $\varepsilon_{r,\text{comp}}(\text{target}) := \overline{R} \cdot \varepsilon_r$ (bckgr). Here 'a/b' means 'above/below the ground'. For 'a' and 'b' the background is air and dry sand, respectively.

Target	a/b	$\overline{R}$	ε_r(bckgr)	$\varepsilon_{r,\text{comp}}$ (target)	$\varepsilon_{r,\text{publ}}$ (target)
Figure 6(a)	–	3.8	1	3.8	4, figure 6(a)
Bush	a	6.4	1	6.4	$\in [3, 20]$, see [20]
Wood stake	a	3.8	1	3.8	$\in [2, 6]$, see [44]
Metal box	b	3.8	$\in [3, 5]$, see [44]	$\in [11.4, 19]$	$\in [10, 30]$, see (7.2)
Metal cylinder	b	4.3	$\in [3, 5]$, see [44]	$\in [12.9, 21.4]$	$\in [10, 30]$, see (7.2)
Plastic cylinder	b	0.28	$\in [3, 5]$, see [44]	$\in [0.84, 1.4]$	1.2, see [45]

in values of $\overline{R}$, which were within tabulated limits (corresponding images are not shown for brevity); also see section 9 for a discussion of this issue.

Test 3. *The image of a wood stake* (see figures 4(c) and 5(b)). The computed image is displayed in figure 7(e).

Test 4. *The image of a metal box* (see figures 4(e) and 5(b)). The computed image is displayed in figure 7(f).

Since we had total five sets of data in our possession, we also imaged two more cases: plastic cylinder and metal box, both buried in soil. Dielectric constants were not measured when the data were collected. Therefore, we compared computed values of dielectric constants with those listed in tables [44, 45]. Note that these tables often provide a range of values rather than exact numbers. The soil was dry sand, where the dielectric constant varies between 3 and 5 [44]. Denote $\varepsilon_{r,\text{publ}}$ (target) the published value of the dielectric constant for non-metallic targets. By (7.2) we regard $\varepsilon_{r,\text{publ}}(\text{target}) \in [10, 30]$ for metals. The case of bush (vegetation) is not listed in [44, 45]. Hence, we took $\varepsilon_{r,\text{publ}}(\text{target})$ for vegetation from figures 2 and 3 of [20]. Table 1 summarizes our results.

9. Discussion

Since dielectric constants were not measured in experiments, the maximum that can be done is to compare computational results with tabulated values (also, see the last paragraph of this section). Therefore, the *most important* conclusion from table 1 is that computed dielectric

29

constants of targets fall well within tabulated limits for five out of five available data sets. This was achieved regardless of the significant limitations of our data. Naturally, these limitations have resulted in a large and yet unknown noisy component in the data, which we have used as inputs for our algorithm. Thus, we conclude that the above results point towards the robustness of our algorithm.

Because of the discussion of this section, it is worth summarizing now the severe limitations of our data.

(1) Time-resolved signals were integrated and averaged over radar/target distances between 20 and 8 m and then averaged with respect to two sources and 16 detectors.
(2) A huge misfit between experimentally measured and computationally simulated data.
(3) The 3D reality versus the necessity to model the process as 1D: because we had only one time-resolved curve for each target.
(4) The need to use only one 1D hyperbolic PDE for modeling the process instead of the full Maxwell system: because only one component of the electric field was measured.
(5) A number of other uncertainties listed in subsection 7.2.

It is unlikely that an accurate image of a 3D target can be calculated using only a single time-dependent curve (item 3). Therefore, given the above limitations, we had only a *very limited goal* in this study. More precisely, this goal was to calculate a single number for each target, which would characterize the target/background ratio of dielectric constants, and, at the same time, would fall within tabulated limits. That number is $\overline{R}$. We point out that the number $\overline{R}$ is still computed by first computing the function $R(x)$ in (7.1).

The data pre-processing procedure, which was similar to that of subsection 7.3, was used in [10, 26] and in chapter 5 of [6]. Similar to subsection 7.3, only one peak for each time-resolved curve was singled out in [6, 10, 26]. In that case transmitted (rather than backscattering) time-resolved experimental data were measured on many detectors that were located on a piece of a plane. Because those data were collected on a piece of a plane, it was possible to compute 3D images by a 3D analogue of the algorithm of this paper. The data of [6, 10, 26] were collected in a controlled laboratory environment, unlike the data of this paper, which were collected in the uncontrolled environment in the field. Another important element, which led to some differences with the method of subsection 7.3, was that the reference signal (i.e. the one for the free space) was measured in [6, 10, 26]. The latter is not our case. Also, unlike this paper, refractive indices $n = \sqrt{\varepsilon_r}$ of targets were directly measured *a posteriori*, i.e. after computational results were obtained. In other words, refractive indices were computed for the most difficult *blind* data case. Very accurate reconstructions of both refractive indices and locations of targets were obtained in [6, 26]. Tables 5 and 6 in [26] as well as tables 5.4 and 5.5 in [6] show only a few per cent difference between computed and directly measured refractive indices in six out of six cases. Next, the so-called adaptivity technique [3, 4] has refined images. The adaptivity has provided quite accurate reconstructions of all three components of targets: refractive indices, locations and shapes; see [10] and figures 5.13–5.16 in [6]. We point out that the adaptivity has used the solution of the approximately globally convergent algorithm as the starting point. There is no reason to apply the adaptivity to the data of this paper, because of the 3D reality versus the 1D mathematical model (see item 3 above).

Since the data pre-processing procedure of subsection 7.3 results only in a single peak to work with, it might miss some important yet unknown pieces of information. Still, because of the analogy of this procedure with that of [6, 10, 26], we believe that the resulting pre-processed data of figure 5(b) are sufficient for the very limited goal given above. We believe that table 1 indicates that we have achieved that goal. It remains to be seen whether the number $\overline{R}$ can be satisfactory computed by some other techniques if using our data.

The scaling number $SN = 10^{-7}$, which we chose on the basis of considerations of subsection 7.3, might not be an optimal one. Hence, we conducted a limited sensitivity study to see how sensitive $\overline{R}$ is to the choice of scaling number; see test 2 in section 8. We found that variations of SN by 20%, $SN = 0.8 \times 10^{-7}$ and $SN = 1.2 \times 10^{-7}$ result in values of $\overline{R}$, which are still within tabulated limits for all five targets we worked with. An optimal value of SN might likely be computed via comparison of values of $\overline{R} := \overline{R}(SN)$ with the directly measured value of $\overline{R}$ for a few targets. Next, the so-chosen SN should be used for all other targets. At this point, however, we are not in a position to do this because of the absence of direct measurements of dielectric constants of the above targets.

A more complete understanding of the capability of our algorithm to work with more complicated targets as well as a better understanding of its accuracy limits for this kind of experimental data will be one of the topics of our future research effort. In particular, that effort will likely include a more sophisticated data pre-processing procedure, which would result in a bigger information content being extracted from each experimental curve.

The recovered dielectric constant by itself is not sufficient information to distinguish one target from another. The purpose of estimating the dielectric constant is to provide one extra piece of information about the target. Indeed, up to this point, most of the radar community relies solely on the intensity of the radar image for the detection and discrimination of targets. It is hoped therefore that when the intensity information is coupled with the new dielectric information, algorithms can then be designed that will ultimately provide better performance in terms of probability of detection and false alarm rate. As is clear from table 1, some targets will have dielectric values that tend to group together, but even that is useful information. For example, if the estimated dielectric value is consistent with a plastic land mine, then this would be another clue to uncovering the target.

In summary, we believe that the results of this paper indicate that our algorithm is capable of stably and reliably calculating both the function $R(x)$ and the number $\overline{R}$ from the experimental data above. On the next step of this research one should directly measure values of dielectric constants of targets and then compare measured and computational results. Such a study might clarify at least some questions discussed above in this section. However, the process of collection of the above experimental data is both expensive and time consuming. This is the reason why we do not have any other experimental data at the moment. Still, we might well get them in the future.

References

[1] Alekseenko N V, Burov V A and Rumyantseva O D 2008 Solution of the three-dimensional acoustic inverse scattering problem. The modified Novikov algorithm *Acoust. Phys.* **54** 407–19
[2] Bateman H and Erdelyi A 1954 *Tables of Integral Transforms* vol 1 (New York: McGrawHill)
[3] Beilina L and Johnson C 2001 A hybrid FEM/FDM method for an inverse scattering problem *Numerical Mathematics and Advanced Applications: ENUMATH 2001* (Berlin: Springer) pp 4–15
[4] Beilina L and Johnson C 2005 *A posteriori* error estimation in computational inverse scattering *Math. Models Methods Appl. Sci.* **15** 23–37

[5] Beilina L and Klibanov M V 2008 A globally convergent numerical method for a coefficient inverse problem *SIAM J. Sci. Comput.* **31** 478–509

[6] Beilina L and Klibanov M V 2012 *Approximate Global Convergence and Adaptivity for Coefficient Inverse Problems* (New York: Springer)

[7] Beilina L and Klibanov M V 2010 Synthesis of global convergence and adaptivity for a hyperbolic coefficient inverse problem in 3D *J. Inverse Ill-posed Problems* **18** 85–132

[8] Beilina L and Klibanov M V 2010 *A posteriori* error estimates for the adaptivity technique for the Tikhonov functional and global convergence for a coefficient inverse problem *Inverse Problems* **26** 045012

[9] Beilina L, Klibanov M V and Kokurin M Yu 2010 Adaptivity with relaxation for ill-posed problems and global convergence for a coefficient inverse problem *J. Math. Sci.* **167** 279–325

[10] Beilina L and Klibanov M V 2010 Reconstruction of dielectrics from experimental data via a hybrid globally convergent/adaptive algorithm *Inverse Problems* **26** 125009

[11] Beilina L, Kuzhuget A V and Klibanov M V 2011 New *a posteriori* error estimates for adaptivity technique and global convergence for the hyperbolic coefficient inverse problem *J. Math. Sci.* **172** 449–76

[12] Beilina L and Klibanov M V 2012 The philosophy of the approximate global convergence for multidimensional coefficient inverse problems *Complex Variables and Elliptic Equ.* at press

[13] Bikowski J, Knudsen K and Mueller J L 2011 Direct numerical reconstruction of conductivities in three dimensions using scattering transforms *Inverse Problems* **27** 015002

[14] Born M and Wolf E 1999 *Principles of Optics: Electromagnetic Theory of Propagation, Interference and Diffraction of Light* (Cambridge: Cambridge University Press)

[15] Bourgeois L and Darde J 2010 A duality-based method of quasi-reversibility to solve the Cauchy problem in the presence of noisy data *Inverse Problems* **26** 095016

[16] Burov V A, Morozov S A and Rumyantseva O D 2002 Reconstruction of fine-scale structure of acoustical scatterers on large-scale contrast background *Acoust. Imaging* **26** 231–8

[17] Burov V A, Alekseenko N V and Rumyantseva O D 2009 Multifrequency generalization of the Novikov algorithm for the two-dimensional inverse scattering problem *Acoust. Phys.* **55** 843–56

[18] Cao H, Klibanov M V and Pereverzev S V 2009 A Carleman estimate and the balancing principle in the quasi-reversibility method for solving the Cauchy problem for the Laplace equation *Inverse Problems* **25** 35005

[19] Chadan K and Sabatier P C 1989 *Inverse Problems in Quantum Scattering Theory* (New York: Springer)

[20] Chuah H T, Lee K Y and Lau T W 1995 Dielectric constants of rubber and oil palm leaf samples at X-band *IEEE Trans. Geosci. Remote Sens.* **33** 221–3

[21] DeAngelo M and Mueller J L 2010 2-D ∂-bar reconstructions of human chest and tank using an improved approximation to the scattering transform *Physiol. Meas.* **31** 221–32

[22] Engl H W, Hanke M and Neubauer A 2000 *Regularization of Inverse Problems* (Boston, MA: Kluwer)

[23] Friedman A 1964 *Partial Differential Equations of Parabolic Type* (Englewood Cliffs, NJ: Prentice-Hall)

[24] Isaacson D, Mueller J L, Newell J C and Siltanen S 2006 Imaging cardiac activity by the D-bar methods for electrical impedance tomography *Physiol. Meas.* **27** S43–50

[25] Kabanikhin S I and Shishlenin M A 2011 Numerical algorithm for two-dimensional inverse acoustic problem based on Gel'fand–Levitan–Krein equation *J. Inverse Ill-Posed Problems* **18** 979–95

[26] Klibanov M V, Fiddy M A, Beilina L, Pantong N and Schenk J 2010 Picosecond scale experimental verification of a globally convergent numerical method for a coefficient inverse problem *Inverse Problems* **26** 045003

[27] Klibanov M V, Bakushinsky A B and Beilina L 2011 Why a minimizer of the Tikhonov functional is closer to the exact solution than the first guess *J. Inverse Ill-Posed Problems* **19** 83–105

[28] Klibanov M V, Su J, Pantong N, Shan H and Liu H 2010 A globally convergent numerical method for an inverse elliptic problem of optical tomography *Appl. Anal.* **89** 861–91

[29] Klibanov M V and Timonov A 2004 *Carleman Estimates for Coefficient Inverse Problems and Numerical Applications* (Utrecht: VSP)

[30] Kuzhuget A V and Klibanov M V 2010 Global convergence for a 1-D inverse problem with application to imaging of land mines *Appl. Anal.* **89** 125–57

[31] Kuzhuget A V, Pantong N and Klibanov M V 2011 A globally convergent numerical method for a coefficient inverse problem with backscattering data *Methods Appl. Anal.* **18** 47–68

[32] Ladyzhenskaya O A, Solonnikov V A and Uralceva N N 1968 *Linear and Quasilinear Equations of Parabolic Type* (Providence, RI: American Mathematical Society)

[33] Lattes R and Lions J-L 1969 *The Method of Quasireversibility: Applications to Partial Differential Equations* (New York: Elsevier)

[34] Lavrentiev M M, Romanov V G and Shishatskii S P 1986 *Ill-Posed Problems of Mathematical Physics and Analysis* (Providence, RI: American Mathematical Society)

[35] Levitan B M 1987 *Inverse Sturm–Liouville Problems* (Utrecht: VSP)

[36] Nguyen N, Wong D, Ressler M, Koenig F, Stanton B, Smith G, Sichina J and Kappra K 2007 Obstacle avoidance and concealed target detection using the Army Research Lab ultra-wideband synchronous impulse Reconstruction (UWB SIRE) forward imaging radar *Proc. SPIE* **6553** 65530H(1)–(8)

[37] Novikov R G 1988 Multidimensional inverse spectral problem for the equation $-\triangle\psi + (v(x) - Eu(x))\psi = 0$ *Funkc. Anal. Priloz.* **2284** 11–22

[38] Novikov R G 1992 The inverse scattering problem on a fixed energy level for the two-dimensional Schrödinger operator *J. Funct. Anal.* **103** 409–63

[39] Novikov R G 2005 The ∂-bar approach to approximate inverse scattering at fixed energy in three dimensions *Int. Math. Res. Pap.* **6** 287–349

[40] Novikov R G 2009 An effectivization of the global reconstruction in the Gel'fand–Calderon inverse problem in three dimensions *Contemp. Math.* **494** 161–84

[41] Pantong N, Su J, Shan H, Klibanov M V and Liu H 2009 Globally accelerated reconstruction algorithm for diffusion tomography with continuous-wave source in an arbitrary convex shape domain *J. Opt. Soc. Am.* A **26** 456–72

[42] Shan H, Klibanov M V, Su J, Pantong N and Liu H 2008 A globally accelerated numerical method for optical tomography with continuous wave source *J. Inverse Ill-Posed Problems* **16** 765–92

[43] Su J, Klibanov M V, Liu Y, Lin Z, Pantong N and Liu H 2011 An inverse elliptic problem of medical optics with experimental data http://www.ma.utexas.edu/mp_arc/

[44] Tables of dielectric constants at http://www.asiinstr.com/technical/Dielectric0Constants.htm

[45] Tables of dielectric constants at http://www.krohne.com/Dielectric_Constants.6840.0.html

[46] Tikhonov A N, Goncharsky A V, Stepanov V V and Yagola A G 1995 *Numerical Methods for the Solution of Ill-Posed Problems* (London: Kluwer)

[47] Xin J, Beilina L and Klibanov M V 2010 Globally convergent numerical methods for coefficient inverse problems for imaging inhomogeneities *Comput. Sci. Eng.* **12** 64–77